Determination of the refractory enrichment factor of the bulk silicate Earth from metal-silicate experiments on rare Earth elements

P. Faure, M. Boyet, Mohamed Ali M.A. Bouhifd, Geeth Manthilake, T. Hammouda, J.-L. Devidal

▶ **To cite this version:**

P. Faure, M. Boyet, Mohamed Ali M.A. Bouhifd, Geeth Manthilake, T. Hammouda, et al.. Determination of the refractory enrichment factor of the bulk silicate Earth from metal-silicate experiments on rare Earth elements. Earth and Planetary Science Letters, 2021, pp.116644. 10.1016/j.epsl.2020.116644 . hal-03004013

HAL Id: hal-03004013
https://uca.hal.science/hal-03004013

Submitted on 13 Nov 2020

HAL is a multi-disciplinary open access archive for the deposit and dissemination of scientific research documents, whether they are published or not. The documents may come from teaching and research institutions in France or abroad, or from public or private research centers.

L'archive ouverte pluridisciplinaire **HAL**, est destinée au dépôt et à la diffusion de documents scientifiques de niveau recherche, publiés ou non, émanant des établissements d'enseignement et de recherche français ou étrangers, des laboratoires publics ou privés.

Copyright

Determination of the refractory enrichment factor of the bulk silicate Earth from metal-silicate experiments on Rare Earth Elements

P. Faure[1], M. Boyet[1*], M.A. Bouhifd[1], G. Manthilake[1],

T. Hammouda[1] and J.-L. Devidal[1]

[1]Laboratoire Magmas et Volcans, Université Clermont Auvergne, CNRS UMR 6524,

OPGC-IRD, F-63000 Clermont-Ferrand, France

*Corresponding authors: maud.boyet@uca.fr

Abstract

This study investigates the partitioning of rare earth elements (REE) from La to Gd between molten metal and silicate to evaluate potential fractionation occurring during core-mantle differentiation. We report molten metal-silicate liquid partition coefficients from 24 multi-anvil experiments, extending the range of pressure, previously ranging from 1 to 8 GPa, up to 14 GPa. Experiments were performed at temperatures of between 2300 and 2560 K, and for oxygen fugacities ranging from the IW (Iron-Wüstite buffer) to IW –4. Metal-silicate partition coefficients for the studied REE vary with the oxygen fugacity and S concentration in the metallic phase of the system. These elements were all lithophile during the Earth's accretion. By compiling all existing data on molten metal-silicate liquid partitioning, REE partitioning between the mantle and core during the Earth's accretion can be determined for a wide range of P, T and fO_2 conditions representing the early evolution of planetary bodies from planetesimals to planets. REE concentrations of the bulk silicate Earth (BSE) are calculated from accretion scenarios using varying proportions and compositions of chondritic building blocks. The models

selected are those that reproduce the Earth's nucleosynthetic isotope signature and the Ni/Co, Th/U and Nb/Ta ratios of the BSE. The BSE refractory element enrichment factor determined from REE data is equal to 2.88 (relative to CI chondrites). This calculation takes into account the depletion in volatile elements in the Earth compared to chondrites. This new estimate is in good agreement with previous determinations based on analysis of the upper mantle rocks, which supports the idea of a chemically homogeneous mantle. We also confirm that the formation of the core, with or without segregation of a sulfide phase, does not fractionate Sm/Nd and cannot be responsible for the ^{142}Nd excess measured in modern terrestrial samples relative to chondrites.

1. Introduction

The planets of our Solar System result from the accretion of smaller objects including differentiated protoplanetary bodies and primitive objects formed in the early Sun's protoplanetary disk. The bulk chemical compositions of differentiated objects, which are composed of a metallic core surrounded by a silicate reservoir, are difficult to estimate because we do not have access to all the different reservoirs. Core-mantle differentiation processes concentrate chemical elements in the different reservoirs according to their partition coefficients. Siderophile elements are preferentially drawn into the metallic core whereas lithophile elements remain in the silicate portion. Chondrites, which escaped planetary differentiation, are commonly used as a reference for elements characterized by a high condensation temperature called refractory elements. Unlike volatile elements, they must not have been partially lost during the accretion stage. Then planetary bodies should retain chondritic ratios of refractory lithophile elements (RLE) in their silicate parts. Ratios of two elements characterized by a high condensation temperature (e.g. Ca, Al, rare earth elements) are similar in the different chondrite groups (Wasson and Kallemeyn, 1988). This observation forms the basis for many geochemical models used for reconstructing the composition of the bulk silicate Earth (BSE). Proposed BSE compositions have chondritic RLE ratios, and the absolute concentrations in the BSE for these elements are commonly expressed in the literature using the enrichment factor (EF), which is the BSE to CI concentration ratio ($EF=[RLE]_{BSE}/[RLE]_{CI}$). This enrichment factor is usually determined from the concentrations measured for highly refractory elements (e.g. Al, Ti) in the most fertile upper mantle rocks. Once determined, it is applied to all RLE to calculate the BSE composition. Enrichment factors are in the range of 1.7 to 2.8 in the literature

59 explaining the differences in published BSE compositions (Lyubetskaya and Korenaga,
60 2007; McDonough and Sun, 1995; Palme and O'Neill, 2014). Concentrations in heat-
61 producing elements vary by ~20% in the different BSE models with important
62 implications on the geodynamics and habitability of Earth (Jellinek and Jackson 2015).
63
64 The absence of RLE fractionation during the early phase of the Earth's evolution has
65 been challenged, due to the presence of small $^{142}Nd/^{144}Nd$ excesses in modern terrestrial
66 samples relative to chondrites (up to 30 parts per million in the $^{142}Nd/^{144}Nd$ ratio
67 depending of the chondrite group; Boyet and Carlson, 2005). Since ^{142}Nd is a radiogenic
68 isotope partly produced by the decay of ^{146}Sm ($T_{1/2}$=103 Ma), a very early
69 differentiation event of the silicate Earth had been proposed to explain this offset (Boyet
70 and Carlson, 2005). Variation in the $^{142}Nd/^{144}Nd$ ratio measured between the different
71 groups of chondrites reflects nucleosynthetic heterogeneities in the protoplanetary disk
72 during the accretion stage (Boyet et al., 2018). However, variations in mass-independent
73 stable isotope ratios for Nd ($^{145}Nd/^{144}Nd$, $^{148}Nd/^{144}Nd$ and $^{150}Nd/^{144}Nd$) are too small to
74 be clearly resolved, with the exception of carbonaceous chondrites (Saji et al., 2016).
75 The smallest difference in ^{142}Nd between chondrite and terrestrial samples is for the
76 enstatite chondrite group (average value -10 ppm, Boyet et al., 2018). Enstatite
77 chondrites (EC) display nucleosynthetic isotope signature similar to BSE for a large
78 number of isotope systematics suggesting that they represent a large fraction of the
79 material accreted to form the Earth (e.g. Dauphas 2017). Because the analytical
80 precision is not sufficient to detect significant variations in other Nd isotope ratios in
81 EC relative to the terrestrial reference, a radiogenic origin of the ^{142}Nd excess measured
82 in modern terrestrial samples cannot be totally disproved. In this case the small excess

of ^{142}Nd in modern terrestrial samples relative to chondrites could be the result of Sm/Nd fractionation produced during the lifetime of the parent isotope, i.e. during the first 500 Ma of Solar System history.

The Earth's core was proposed by Andreasen et al. (2008) as a potential enriched reservoir (early-formed low Sm/Nd reservoir characterized by deficit in ^{142}Nd), even though no REE partition coefficients were available then for core-forming conditions. While experimental data suggest that Sm and Nd remain lithophile and behave in a similar fashion during liquid metal – liquid silicate partitioning (Bouhifd et al., 2015), it has been proposed that the addition of a significant amount of S into the core would fractionate Sm and Nd enough to explain the small ^{142}Nd excess in modern terrestrial samples relative to chondrites (Wohlers and Wood, 2015). A small number of recent experiments performed at higher temperature (2100°C), more compatible with core formation conditions, seems to rebut elemental fractionation between Sm and Nd in a sulfur-rich environment (Wohlers and Wood, 2017). To further constrain the behaviour of REE during core-mantle differentiation processes, we report molten metal-silicate liquid partition coefficients (D) determined from 24 multi-anvil experiments. We extended the range of pressure to 14 GPa, as previous measurements had only been carried out between 1.5 and 8 GPa. Experiments were performed from 2300 to 2560 K, and for oxygen fugacity conditions ranging from IW (Iron-Wüstite buffer) to IW-4. Partition coefficients were determined for REE from La to Gd in a liquid metal-liquid silicate system with various amounts of S. Our new data set, combined with all existing experimental results, give a consistent parameterisation of the behaviour of these elements during magma ocean episodes for planetary bodies of different sizes

(planetesimals to planets) and for compositions representing the diversity found in the inner Solar System.

2. Experimental methods

2.1. Starting materials

The starting material for the silicate consisted of a natural equilibrated EC from the EL6 subgroup (Hvittis, composition given by Rubin, 1983). Once finely ground, the powder was doped with the studied elements, at a level ranging from 1500 ppm to 1 wt% per REE. Since the field of application of Henry's law is not well defined for REE, we decided to split the studied REE into two different doping solutions , synthesized from AAS standard solutions, in order to minimize the amount of trace elements in the starting materials. Type A solution contained La, Ce, Pr, Nd and Sm, while type B solution contained Nd, Sm, Eu and Gd. For sulfur-rich experiments, a type C solution containing all 7 REE from La to Gd at a level of 1500 ppm each was synthesized. All solutions contained Nd and Sm in order to compare our experiments with previous studies (Bouhifd et al., 2015; Wohlers and Wood, 2017).

Various amounts of Fe-rich alloys (in the Fe–Ni–Si–S system) were then added in a weight proportion of 50:50. Control of the fo_2 between IW to IW-4 was obtained by addition of metallic Si to the starting material, resulting in the reduction of the FeO present in the silicate phase from about 20 wt% to ~0.2 wt% in some run-products. Each composition was mixed and ground in ethanol, before being dried and stored in a vacuum sealed dessicator for at least 48 h.

2.2. High-pressure and high-temperature syntheses

High-pressure and high-temperature experiments were carried out using the 1000-ton and 1500-ton multi-anvil apparatuses installed at the French National High-Pressure facility of Laboratoire Magmas et Volcans (LMV) in Clermont-Ferrand. Experimental conditions are summarised in Table 1, based on pressure calibrations similar to those already described in Boujibar et al., (2014) and Hammouda (2003). The pressure assemblies consisted of Cr-doped MgO octahedra, 18 or 14 mm edge length, containing a stepped graphite or $LaCrO_3$ heater, respectively. Octahedra were compressed using 32 mm tungsten carbide anvils with truncation edge lengths of 11 and 8 mm (with 18 and 14 mm octahedra, respectively) and pyrophyllite gaskets. The samples were contained either in graphite for 6 GPa experiments or in MgO single crystal capsules for 14 GPa experiments. The assembled octahedra were dried in an oven at 500 K overnight before each experiment. The samples were first compressed to the target pressure at room temperature and then heated to the desired temperature (between 2300 and 2560 K) for durations of 2 to 4 min. These durations are sufficient to achieve equilibrium between silicate melt and metallic liquid (e.g. Boujibar et al., 2014; Faure et al., 2020; Siebert et al., 2011) while preventing excessive reaction between the capsule and the silicate or metallic phases. Textural and chemical evidences (uniformed quenched silicate melts, well-formed metal blobs, chemically homogeneous metallic and silicate phases) confirmed that equilibrium was achieved in the sample. Temperatures were monitored with a thin axial $W_5Re/W_{26}Re$ thermocouple whose junction was in direct contact with the top of the capsule. In the event that the thermocouple was lost, the temperature was determined using the power/temperature relation determined in previous experiments. The pressure and temperature uncertainties are estimated to be ±1 GPa and ± 100 K

155 respectively, since no pressure correction was made for the emf of the thermocouple
156 (e.g. Li et al., 2003). The samples were quenched by shutting off the power, which
157 resulted in a quench rate of approximately 800 K/s. The samples were then
158 decompressed over a period of about 12h. After the experiment, the run-product was
159 mounted in epoxy, polished and carbon coated for the chemical analyses.
160
161 **2.3. Electron Microprobe**
162 Major and minor elements in the metal and silicate phases were analyzed using the
163 LMV CAMECA SX100 electron microprobe using a 20 kV accelerating voltage. Major
164 elements analyses in the silicate phase were performed at 50 nA with a 5-20 μm
165 defocused beam, counting times on the peak ranging from 5 to 80 seconds depending on
166 element concentrations and detection limit requirements. The standards for silicates
167 were natural minerals and synthetic oxides (Si, Ca: wollastonite; Mg: forsterite; Al:
168 Al_2O_3; Fe: fayalite; Na: albite; K: orthoclase; Ti, Mn: $MnTiO_3$; Cr: Cr_2O_3; Ni: NiO). For
169 metallic and sulfide phase analyses, we used a defocused beam (10–20 μm), beam
170 currents of 15 nA for the major elements (Fe, Ni, S and Si) and 150 nA for the trace
171 elements, and counting times on the peak ranging from 5 to 60 s. Standards were pyrite
172 for Fe and S in sulfides, and pure metal (Fe, Mn, Si, Mg, Ni, Cr) for metallic alloys. For
173 samples embedded in graphite capsules, the carbon content in Fe-alloys was estimated
174 from the deviation of the analyses totals from 100%.
175
176 **2.4. Laser Ablation ICP-MS**
177 Trace element concentrations were determined using the LMV Elements XR laser-
178 induced coupled plasma-mass spectrometer (LA ICP-MS) coupled with a 193 nm ArF

179 excimer type laser (Resonetics M-50). The laser was fired at selected sample regions at
180 a repetition rate of 2 to 4 Hz with 4 mJ output energy beam, with a spot size diameter of
181 15–44 μm in the silicate, and 80-130 μm in the metal. Ablation duration lasted usually
182 around 80 s and was done in a pure He atmosphere. Reference material glasses NIST
183 SRM 610, NIST 612 and BCR2-G were used for external calibration (Gagnon et al.,
184 2008), and ^{29}Si, ^{57}Fe and ^{60}Ni were used as internal calibrators. All data were processed
185 using the GLITTER software package (Achterberg et al., 2001). Ca signal was
186 monitored during metal analyses and Fe and Ni signals during silicate analyses. Any
187 sudden variation in their content was considered as indicative of phase contamination
188 (metal contamination during the silicate phase analysis, or vice versa) and the
189 corresponding analyses were rejected.
190
191 **2.5 Oxygen fugacity determination**
192 Oxygen fugacity was calculated using the Fe and FeO contents of the metal and silicate
193 quenched phases, using the equilibrium reaction:
194 $Fe^{metal} + ½\ O_2 \leftrightarrow FeO^{silicate}$ (1)
195 The fo_2 was estimated relative to the Iron-Wüstite buffer (IW) from the activities of Fe
196 and FeO in the metal and silicate following the equation:
197 $$\log fo_2(\Delta IW) = 2 \times \log\left(\frac{a_{FeO}^{sil}}{a_{Fe}^{met}}\right) \quad (2)$$
198 where $a_{FeO}^{sil} = \gamma_{FeO}^{sil} \times X_{FeO}^{sil}$ and $a_{Fe}^{met} = \gamma_{Fe}^{met} \times X_{Fe}^{met}$ represent the activity of FeO in the
199 silicate liquid and Fe in the metal phase, respectively. X_{Fe}^{met} and X_{FeO}^{sil} are the molar
200 fractions of Fe in the metallic phase and FeO in the silicate liquid. γ_{FeO}^{sil} and

201 γ_{Fe}^{met} represent the activity coefficient of FeO in the silicate liquid, and the activity of Fe
202 in the metallic phase, respectively.
203 The Fe activity coefficient in Fe-rich alloys was calculated from the formula of Ma
204 (2001), using the interaction parameters ε provided Wade and Wood (2005) and the
205 activity calculator (http://www.earth.ox.ac.uk/~expet/metalact/) provided by the
206 University of Oxford.
207 We used the average gamma value derived from studies at 1 bar by O'Neill and Eggins
208 (2002) for several melt compositions in the CaO-MgO-Al_2O_3-SiO_2 system, and by
209 Holzheid et al. (1997) for melts in the anorthite-diopside system and komatiitic basalt,
210 assuming no pressure effect on the activity coefficients in silicate melts (Toplis, 2004).
211

212 **3. Results**

213 **3.1. Phase assemblages and compositions**

214 Typical run products consisted of quenched silicate melts and liquid metal blobs (Figure
215 1). Measured chemical compositions of the quenched silicate and metallic melts are
216 reported in Appendix A. The run-product microstructures show that both phases became
217 fully molten during the high pressure and high temperature experiments. The metallic
218 phase generally forms a large "core" located at the center or to one side of the capsule
219 or, less frequently, large drops distributed throughout the sample. In some cases,
220 dendritic microstructures are observed in the silicate, requiring a defocused beam for
221 chemical analyses to average the heterogeneous quenched textures. Several criteria are
222 used to demonstrate the thermodynamic equilibrium of these experimental samples: (i)
223 multiple analyses in the silicate phase show that it is homogeneous with no evidence of

chemical zoning, and (ii) all metal blobs embedded in the silicate matrix have identical composition within uncertainties.

In the present study we also tested the effect of the nature of the capsule (graphite vs. MgO single crystal) on REE partitioning. Using graphite capsules, analytical totals for the metallic phases indicate some amount of C dissolved in the metal (from 0.21 to 4.99 wt%, see Appendix A1). More details about the dissolution of C into the metallic phases are reported in Appendix A2. On the other hand, the MgO single crystal capsule tends to saturate the silicate phase in MgO, leading to the formation of olivine quenched crystals instead of enstatite in these samples. Previous studies based on multi-anvil and piston-cylinder experiments (Bouhifd et al., 2015; Wohlers and Wood, 2017) showed that these interactions do not have a significant effect on the partitioning of REE. In addition, we observed no noticeable difference in REE molten metal-silicate liquid partition coefficients between 14 GPa (MgO single crystal capsule) and 6 GPa (graphite capsule) experiments for a similar range of temperature, fO_2 and chemical composition, showing no significant impact of the nature of the capsule or pressure in our experiments (Appendix B).

3.2. Experimental partition coefficients

Overall, 24 experiments were performed, resulting in 24 new partition coefficients for Sm and Nd and 15 for La, Ce, Pr, Eu and Gd (Table 1). Molten metal – silicate liquid partitioning are always low, ranging from 10^{-3} to 10^{-6}, in agreement with results obtained in previous studies for experiments performed at similar conditions (see Appendix C). The two main parameters influencing liquid metal - liquid silicate

248 partition coefficients are the oxygen fugacity and the sulfur content of the metallic
249 phase. Changing the oxygen fugacity conditions from IW-4 to IW-1 leads to a decrease
250 in the partition coefficient by two to three orders of magnitude (Figure 2 and Appendix
251 D.1). On the other hand, the transition from pure Fe metal to pure FeS increases the
252 partition coefficient of all studied REE by up to three orders of magnitude (Figure 3 and
253 Appendix D.2).
254
255 Europium behaves slightly differently to other studied REE in our experimental
256 conditions (Figures 2-4). Around the Iron-Wüstite buffer, more than 50 % Eu is divalent
257 in a basaltic melt (Burnham et al., 2015). Thus, in the redox conditions of the present
258 study, Eu is mainly in a +2 valence state. Eu^{2+} is more stable in a sulfide phase than all
259 the other trivalent REE, as shown in all the FeS-bearing experiments in this study
260 (Figure 4). In all sulfur-rich samples, the sulfide phase is enriched in Eu, leading to a
261 mean D_{Eu} 2.5 times higher than the partition coefficients for the other REE. Values from
262 the literature are also plotted in Figure 4. Results obtained from experiments performed
263 in evacuated silica tubes at temperatures of between 1200 and 1400 °C (Ingrao et al.,
264 2019; Lodders, 1996) are in agreement with our results. These similarities strongly
265 suggest that pressure and temperature have a negligible effect on molten Fe-rich alloy –
266 silicate liquid partitioning of the studied REE (D_{REE}). That D_{REE} is little dependent on
267 temperature can be can be shown by the fact that the free energy of the exchange
268 reactions for REE are not sensitive to the variation of the temperature in the likely range
269 during core formation (details are reported in Appendix D.3).
270

By including experiments from previous studies, it is also possible to analyze the impact of the nature of the silicate phase on the behavior of the studied REE. The NBO/T (Non-Bridging Oxygen per Tetrahedral cations) value is an indicator of melt polymerization, with zero corresponding to a completely polymerized melt (SiO_2 melt) and a value of 4 corresponding to a completely depolymerized melt (Mg_2SiO_4 melt). For roughly similar experimental conditions and metallic compositions, and for a large difference in silicate composition (NBO/T from 0.5 to 3.7, see Appendix A and C), the D_{REE} coefficients are similar within the analytical uncertainties. Furthermore, besides FeO that is directly related to the oxygen fugacity of experiments, we find no significant impact of any of the major oxides that compose the silicate phase on the partition coefficient of the studied REE, for the available dataset. Therefore, data suggest that the silicate melt composition has no significant influence on the REE metal-silicate partition coefficients.

3.3. Parameterisation of the results

Partitioning of an element between metal and silicate phases can be considered as an exchange reaction involving Fe, FeO and the oxidized and reduced components of element M, of valence *n*:

$$MO_{n/2} + \frac{n}{2}\mathrm{Fe} = \frac{n}{2}\mathrm{FeO} + \mathrm{M} \quad (4)$$

By considering the equilibrium for this exchange reaction, it is possible to write the following relationship between $\log(D_M)$ and $\log(fo_2)$ (Righter et al., 2010):

$$\log(D_M) = a\log(fo_2) + b\frac{1}{T} + c\frac{P}{T} + d\log\left(1 - X_{S\,metal}\right) + e \quad (5)$$

293 The *a*, *b*, *c*, and *e* terms relate to valence *n* $\left(a = -\frac{n}{4}\right)$, enthalpy $\left(\frac{\Delta H^{\circ}}{RT}\right)$, volume $\left(\frac{P\Delta V^{\circ}}{RT}\right)$,
294 and entropy $\left(\frac{\Delta S^{\circ}}{R}\right)$, respectively. The empirical term *d* takes into account the effect of
295 sulfur in a metallic liquid (X_{Smetal} is the wt.% of S into the metallic phase), as discussed
296 previously.
297
298 In order to refine the values of *a* and *d* for La, Ce, Nd, Sm, Eu, and Gd, we used all
299 existing data sets for which the partitioning behavior, phase compositions and
300 experimental conditions (temperature, pressure, oxygen fugacity) had been accurately
301 determined. We considered solid silicate for experiments performed at $T <$ melting
302 temperature of the silicate phase (liquidus). The references as well as the conditions (P,
303 T, fo_2) available for each experiment are listed in Appendices A and C. We used a
304 multiple linear regression (approach used by Bouhifd et al., 2015; Faure et al., 2020;
305 Righter et al., 2010) for each element of interest. For every regression, the robustness of
306 each overall model significance was determined using a Fisher-Snedecor test, and a
307 Student test was run to assess the significance of every variable. Results of the two-
308 variable parameterisation for La, Ce, Pr, Nd, Sm, Eu and Gd are summarized in Table 2
309 with their respective standard deviations and determination coefficients. The p-values
310 determined for each variable are also reported. As seen above, only *a* and *d* are relevant
311 to REE partitioning behavior. The parameters *b* and *c*, corresponding respectively to the
312 effect of T and P are found here of no statistical significance, and are therefore set equal
313 to 0. This result reflects the negligible impact that T and P have on D_{REE} (Appendix B),
314 in comparison to the effect displayed by X_{Smetal} and fo_2, within a dataset containing
315 experiments performed up to 14 GPa and 2560 K. While this observation is in
316 agreement and validate previous studies based on a smaller range of P and T (Bouhifd et

al., 2015; Wohlers and Wood, 2017), a dependence on pressure or temperature might be resolved when data obtained from higher pressure experiments will be collected.

The value of parameter *a* being proportional to the valence of one element (equations 5 and 6), the parameterisations proposed here are consistent with all REE being in a +3 valence state within the studied range of oxygen fugacity conditions, with the exception of Eu, which is essentially +2 below the IW buffer. In an S-free system, an oxygen fugacity from IW-5 to IW-2 will lead to a decrease in D_{Nd} from 2.32×10^{-3} to 3.76×10^{-5} and a decrease in D_{Eu} from 3.71×10^{-4} to 2.34×10^{-5} (Figure 2). The effect of the sulfur content of the metal is also noticeable in our parameterisation, leading to an increase of all REE partition coefficients by about three orders of magnitude when the S content in the metallic phase increases from 0 to ~35 wt% at constant oxygen fugacity. For example, at IW-2, D_{Eu} increases from 2.34×10^{-5} to 2.45×10^{-2} and D_{Nd} increases from 3.31×10^{-5} to 2.56×10^{-2} (Figure 3). No noticeable difference is found between Eu and the other REE with respect to the effect of the sulfur content in metal. In the discussion, we will use parameterisations obtained in the range of conditions of the available dataset, in order to establish the partitioning of REE in the conditions of Earth's core formation.

4. Discussion

4.1. Absence of Sm-Nd fractionation during planetary core formation

Previous high pressure – high temperature experiments led to different conclusions concerning the role of core formation on the Sm/Nd ratio of the BSE. Elemental fractionation between Sm and Nd was reported from sulfide-silicate partitioning data in experiments performed at 1.5 GPa and temperatures between 1400 and 1650°C

(Wohlers and Wood, 2015). However, when both phases are molten, this fractionation is no longer observed. This is shown in our study and from published high pressure – high temperature experiment datasets (Figure 5, Bouhifd et al., 2015; Wohlers and Wood, 2017). Sulfide-silicate and metal-silicate partition coefficients for Sm and Nd vary with two parameters: fO_2 conditions and sulfur content. They must be taken into account when calculating Sm and Nd concentrations in bulk planetary silicate reservoirs. A late addition of sulfide (FeS) to the segregating core, as proposed by Wohlers and Wood (2015), would change the final Sm and Nd concentrations of the BSE since the partition coefficients increase by three orders of magnitude from pure Fe metal to pure FeS. However, Sm and Nd cannot be fractionated during core formation in a Solar System planetary body of any size.

4.2. Refractory Lithophile Element enrichment factor for the Earth calculated from metal/silicate partitioning experiments

Concentrations of refractory lithophile elements in the BSE are conventionally estimated by comparing the chemical composition of the most pristine peridotites (xenoliths and peridotite massifs) representative of the upper mantle and that of chondrites. The traditional Earth composition models have been based on CI chondrites because their bulk composition closely matches the composition of the solar photosphere, except for the most volatile elements. REE concentrations in the BSE are commonly defined using the RLE enrichment factor (EF), which is applied to all refractory lithophile elements considered to be present in the BSE (similar to primitive mantle) in chondritic proportions. When expressed relative to the concentration measured in CI chondrites, this RLE factor lies within the range of 1.7 to 2.8 (Table 3).

365 The determination of this EF is a key feature of most BSE model since non-refractory
366 and non-lithophile element concentrations in the BSE are determined via their observed
367 mantle ratio with RLE. Therefore, the enrichment of the BSE in RLE will dictate the
368 concentration of the BSE in all elements.
369 Here we propose a new approach where the RLE enrichment factor is calculated from
370 the experimental molten metal – silicate liquid REE partitioning results. We have
371 developed a model of planetary accretion focusing on the partitioning of REE between
372 the mantle and the core throughout Earth's formation. In this model, the Earth accreted
373 from impactors with a given chemical composition, which then equilibrate (fully or
374 partially) with the magma ocean of the proto-Earth, until the planet obtains its final
375 mass (M_E = $5.97.10^{24}$ kg). All the scenarios result in a fully formed Earth, with a
376 primitive mantle representing 68% of its mass, the core representing the last 32%. The
377 model takes into account the composition of various building blocks potentially
378 involved over the entire history of the Earth's accretion and metal/silicate partitioning
379 data which evolve with core formation conditions (fO_2, pressure, temperature,
380 composition). The accretion model is described in detail in Appendix E.
381
382 The measurement of small variations in mass-independent stable isotope ratios for a
383 large number of elements, also called nucleosynthetic anomalies, provides a real
384 opportunity to investigate the genetic relationship between the different planetesimals
385 and planets. Several mixtures of different building blocks (which differ in nature and
386 proportions) have been proposed in previous studies to match the terrestrial isotopic
387 signature (e.g. Dauphas et al., 2014; Lodders, 2000). Results vary mainly because
388 different studies focused on different elements. However, most of the studies which

integrate a large database of isotopic ratios agree on a major contribution of enstatite chondrites in the mixture with a smaller contribution of carbonaceous chondrites and/or ordinary chondrites (Warren, 2011; Dauphas 2017; Liebske and Khan, 2019). We assume that Earth accreted materials with bulk chondrite composition from known type of meteorites and potential effects of collisional erosion on the chemical composition are not considered (see Palme and O'Neill, 2014).

Among the available models, only those with a mixture of different building blocks (of chondritic composition) that succeed in reproducing the Earth's isotopic signature are considered (e.g. Dauphas, 2017; Warren, 2011). In order to further test the validity of the accretion scenarios, we also studied the evolution of certain element ratios whose molten metal-silicate liquid partitioning behaviour is well constrained in the literature: Ni/Co, Nb/Ta, and Th/U. Accretion scenarios must be able to reproduced these elementary ratios already well established for the BSE (Nb/Ta = 14.0±0.60; Th/U = 3.78±0.12; Ni/Co = 18.90±0.30, Munker, 2003; Palme and O'Neill, 2014; Wipperfurth et al., 2018). The parameterisations used to constrain the behavior of these elements during metal-silicate partitioning are taken from Fischer et al. (2015) for Ni and Co, Cartier et al. (2014) for Nb and Ta and Faure et al., (2020) for U and Th. Of all the accretion scenarios tested, only those reproducing (within 2σ uncertainties) the BSE elemental ratios are considered in the following discussion (Dauphas, 2017; Dauphas et al., 2014; Lodders, 2000; Warren, 2011). These four accepted scenarios contain for the building blocks between 70 and 91% of EC, the rest being made more oxidized (CC or OC) materials (Table 4). Several models involving different building blocks mixture fail

412 at reproducing the BSE elementary ratios (Javoy, 1995; Burbine and O'Brien, 2004;
413 Javoy et al., 2010; Fitoussi and Bourdon, 2012).
414
415 Rare earth element concentrations in the BSE for these four accepted scenarios are
416 reported in Table 4. Enrichment factors (EF) can be calculated from the comparison of
417 these BSE compositions with CI chondrites concentrations. However, it must be noted
418 that none of the measured chondrite compositions have so far succeeded in reproducing
419 the Earth's depletion in volatile elements compared to CI, as the Earth is more depleted
420 in those elements than any known chondrite (Allègre et al., 2001; Braukmüller et al.,
421 2019; Wang et al., 2016). While it has been suggested that the Earth's depletion in
422 volatile elements could be the result of erosion following a giant impact during late
423 accretion (Halliday, 2004; Hubbard and Ebel, 2014), it has also been proposed that this
424 depletion pattern was already present in the Earth's building blocks (Birck et al., 1999;
425 Siebert et al., 2018, and references therein). The depletion of the Earth in volatiles
426 elements, no matter its occurrence in the planet history, would have a direct impact on
427 the concentration of RLE within the BSE. In order to take the impact of volatile
428 depletion on RLE concentrations in the resulting BSE into account, the concentration of
429 volatile elements in chondrites has been recalculated in order to fit the Earth's volatile-
430 element depletion pattern. This concerns volatile and moderately volatile elements, i.e.
431 those with 50% condensation temperatures below 1230 K (Lodders, 2003). The
432 composition of non-refractory elements for each chondrite group has been recalculated,
433 by applying the primitive mantle (BSE) ratios when normalized to Mg (Lyubetskaya
434 and Korenaga, 2007; Palme and O'Neill, 2014). Then, concentrations of all elements
435 were recalculated to reach 100% weight total. The resulting compositions are found to

436 be enriched in RLE compared to measured chondrite compositions by a factor f_{dry}
437 ranging from 1.6 for EH chondrites, to 2.0 for CM chondrites (Appendix E). A
438 weighted average of these f_{dry} factors, depending on the respective proportion of each
439 chondrite composition in the Earth's building blocks (Table 4), was applied to our
440 calculations.
441
442 Calculated enrichment factors are reported in Table 4 for the four accepted scenarios
443 corresponding to those proposed by Dauphas, (2017), Dauphas et al., (2014), Lodders,
444 (2000) and Warren, (2011). Values are identical within error and the average EF_{dry}
445 value is 2.88 (Figure 6). The effect of volatile depletion shown in the figure is
446 significant, increasing the enrichment factor by a value of about 1. Compared to the
447 concentrations given by previous authors (Table 3, Figure 6), our results are in
448 agreement with BSE composition models based on a geo-petrological approach,
449 showing high RLE concentrations (McDonough and Sun, 1995; Palme and O'Neill,
450 2014). McDonough and Sun (1995) use plots of Ca/Yb, Sc/Yb and Sm/Yb of fertile
451 lherzolites (MgO $\leq$ 40.5wt%) against a TiO_2 content of the BSE set at 0.2 wt. % to
452 estimate the absolute proportions (EF=2.75). Palme and O'Neill (2014) use a mass
453 balance approach to calculate the primitive mantle composition. By first estimating the
454 major oxide concentrations in the primitive mantle (MgO, SiO_2 and FeO), they deduce
455 the amount of the two RLE oxides, CaO and Al_2O_3, using their chondritic ratios. They
456 obtain an RLE enrichment factor of 2.83 ±0.23. The two other BSE models presented in
457 Figure 6 yield lower enrichment factors. Lyubetskaya and Korenaga, (2007), by
458 reassessing the peridotite database from McDonough and Sun (1995), obtain an RLE
459 enrichment factor of the BSE of 2.16 ± 0.37. This value overlaps with the EF_{dry} factor

obtained following the model proposed by Dauphas et al. (2014) (Figure 6). The difference with McDonough and Sun, (1995)'s results is due to the statistical treatment of the database, specifically the selection criteria of pristine samples (metasomatism, melt extraction) and the statistical data filtering

In the model proposed by Allègre et al. (2001), concentrations of refractory elements in the BSE are significantly lower and the calculated enrichment factor is within the range of those calculated from models that do not consider the volatility trend of the BSE (open circles in Figure 6). Allègre et al. (2001) use Mg/Si and Al/Mg ratios for the least differentiated sample of Earth's mantle of 0.945 and 0.095, respectively, taken from Hart and Zindler, (1986). Trace element concentrations are then calculated based on the cosmochemical trend shown by carbonaceous chondrites (and sometime other chondrite groups) in a trace element ratio plot. This model requires very few assumptions and succeeds in reproducing the depletion trend of the Earth's volatile elements. However, when estimating the Earth's RLE concentrations using the ratio trends of these elements in chondrites, this method fails to take into account the relative enrichment in refractory elements of the BSE compared to chondrites due to volatile element loss. Thus they obtain a BSE composition enriched in REE by an average of 1.70 ±0.24 compared to CI.

4.3. Generalisation of the enrichment factor to all RLE?

Most BSE models assume fixed chondrite-normalized RLE ratios. While we show that this hypothesis is relevant for REE from La to Gd (except Eu under specific conditions), some elements usually classified as RLE may change their behavior at core-forming

484 conditions (P, T, fo_2). For example, Nb and Ta are both siderophile elements in reduced
485 conditions. Heterogeneous accretion models in which conditions evolve from reduced to
486 oxidized during the Earth's accretion explain the superchondritic Nb/Ta ratio of the
487 BSE (Cartier et al., 2014). Therefore, the RLE enrichment factor presented here should
488 only be used to calculate the abundances of elements that are known to remain
489 lithophile under Earth accretion conditions. Within the REE group, two elements are
490 likely to behave differently: Eu and Yb. Data on heavy REE are available in the study of
491 Ingrao et al. (2019) and Wohlers and Wood (2017). In a similar fashion to Eu in a sulfur
492 rich environment, Yb fractionation occurs in very reduced conditions (IW -5 to -7) and
493 the partial reduction to a +2 valence state has been identified using X-ray Absorption
494 Near Edge Structure measurements (Ingrao et al., 2019). However, since Eu is more
495 sensitive than Yb to a valence change under reduced conditions, and no significant
496 fractionation between Eu and other studied REE is observed, we do not anticipate that
497 core formation would cause an Yb anomaly in the calculated BSE REE pattern.
498 Furthermore, the S content of the Earth's core is considered to be about 2 wt% from
499 geophysical, geochemical and cosmochemical constraints (e.g. (Allègre et al., 2001;
500 Boujibar et al., 2014). There is still debate as to whether the Earth's core acquired its
501 sulfur signature over the entire accretion history, or exclusively in the last 10-20 % of
502 the Earth's accretion (*e.g.* Wood and Halliday, 2005). In order to consider the impact of
503 the accretion of sulfur-rich bodies on the concentration of REE in the different
504 reservoirs, we ran models representing several scenarios involving impactors containing
505 iron sulfide instead of metallic iron, in various proportions (up to 20% of the Earth's
506 mass). No significant variation in REE concentrations or ratios within the BSE is

observed. The addition of sulfide to the Earth's core, at any time during the Earth's accretion, leaves no noticeable trace on the resulting REE concentrations of the BSE.

4.4. Chemical uniformity of present day mantle?

BSE composition models based on the analysis of the upper mantle rocks consider samples from the upper mantle to be chemically representative of the mantle as a whole. However, it has been proposed that a substantial difference exists between a pyrolitic upper mantle and the lower mantle, below the 660 km seismic discontinuity, particularly in terms of Mg/Si and Mg/Fe (Ringwood, 1989). Various evidences have been used to infer a lower mantle chemically distinct from the upper mantle in terms of major and trace elements. Among them, the isotopic and chemical heterogeneities measured in mantle-derived basalts. Measured isotopic ratios support the existence of early-formed chemical heterogeneities that could be preserved in the deepest part of the mantle. Furthermore, the apparent mismatch between laboratory-measured properties in upper mantle composition assemblage and the seismic and other geophysical properties observed in the lower mantle, coupled with the identification of a global seismic discontinuity at 660 km depth and early interpretations of the density of the lower mantle led to the design of a two chemically distinct layers model of Earth's mantle (see Hofmann, 2014 for a review).

However, one compelling observation in favor of a homogeneous mantle is tomographic images showing slabs of oceanic lithosphere descending through the lower mantle (Fukao and Obayashi, 2013). Furthermore, recent studies combining mineral physics data with seismological constraints support the idea that the lower mantle is most likely

pyrolytic and that there is no need for a chemically stratified mantle (Hyung et al., 2016; Zhang et al., 2013). While it has been suggested that the Earth's layers could affect just the bulk mantle trace element budget (Campbell and O'Neill, 2012), our models show that REE abundances estimated for upper mantle samples are well reproduced by the resulting BSE using accretion models with isotopically-supported building block mixing. This supports the argument in favor of a chemically uniform mantle.

5. Conclusion

Molten metal – silicate liquid partitioning data have been obtained from 24 multi-anvil experiments on rare earth elements from La to Gd. These elements are lithophile under the conditions of Earth accretion, with molten metal – silicate liquid partition coefficients ranging from 10^{-2} to 10^{-6}. Their partitioning behaviour is mainly constrained by the oxygen fugacity and the S concentration in the metallic phase of the system. Using our data, together with previously published results, we obtain a two-variable parameterisation for these elements. They are trivalent during the Earth's accretion, even at low oxygen fugacity conditions, with the exception of Eu, which is divalent. Our results show that Sm and Nd are not significantly fractionated by core formation processes over a large range of fO_2 conditions, even in the presence of a large quantity of sulfur. The main impact of core formation is to concentrate the REE within the BSE. The absolute REE concentration in the BSE depends on the nature of the building blocks involved in the accretion scenario. Accretion scenarios using mixtures of chondrites that match the nucleosynthetic signature of the Earth give an average enrichment factor of 2.88 relative to CI. This result takes into account the RLE enrichment of the BSE due to the Earth's depletion in volatile elements compared to

555 chondrites. Our estimate is in good agreement with those of McDonough and Sun
556 (1995) and Palme and O'Neill, (2014), and in favor of a chemically homogeneous
557 present day mantle. This enrichment factor can be extended to other elements which
558 remain strictly lithophile during Earth core formation. The formation of the core, with
559 or without segregation of a sulfide phase, cannot be responsible for the small ^{142}Nd
560 excess measured in modern terrestrial samples relative to chondrites.
561
562 **Acknowledgments**
563 Detailed reviews by two anonymous reviewers are much appreciated as are the editorial
564 comments and handling by James Badro. This project has received funding from the
565 European Research Council (ERC) under the European Union's Horizon 2020 research
566 and innovation program (Grant Agreement No. 682778 – ISOREE). The multi-anvil
567 apparatus of Laboratoire Magmas et Volcans is financially supported by the CNRS
568 (Instrument national de l'INSU). This is also the French Government Laboratory of
569 Excellence Initiative N° ANR-10_LABX-006, the Région Auvergne and the European
570 Regional Development Fund. This is Laboratory of Excellence ClerVolc contribution
571 N° xxx.
572
573 **References**
574 Achterberg, E. van, Ryan, C.G., Jackson, S., and Griffin, W.L. (2001). Data reduction
575 software for LA-ICP-MS. In Laser-Ablation- ICPMS in the Earth Sciences,
576 Principles and Applications, 239–243.
577 Allègre, C., Manhès, G., and Lewin, É. (2001). Chemical composition of the Earth and
578 the volatility control on planetary genetics. Earth and Planetary Science Letters

579 *185*, 49–69.

580 Andreasen, R., Sharma, M., Subbarao, K.V., and Viladkar, S.G. (2008). Where on Earth
581 is the enriched Hadean reservoir? Earth and Planetary Science Letters *266*, 14–28.

582 Birck, J.L., Rotaru, M., and Allègre, C.J. (1999). 53Mn-53Cr evolution of the early
583 solar system. Geochimica et Cosmochimica Acta *63*, 4111–4117.

584 Bouhifd, M.A., Boyet, M., Cartier, C., Hammouda, T., Bolfan-Casanova, N., Devidal,
585 J.L., and Andrault, D. (2015). Superchondritic Sm/Nd ratio of the Earth: Impact of
586 Earth's core formation. Earth and Planetary Science Letters *413*, 158–166.

587 Boujibar, A., Andrault, D., Bouhifd, M.A., Bolfan-Casanova, N., Devidal, J.-L., and
588 Trcera, N. (2014). Metal–silicate partitioning of sulphur, new experimental and
589 thermodynamic constraints on planetary accretion. Earth and Planetary Science
590 Letters *391*, 42–54.

591 Boyet, M., and Carlson, R.W. (2005). 142Nd Evidence for Early (>4.53 Ga) Global
592 Differentiation of the Silicate Earth. Science *309*, 576–581.

593 Boyet, M., Bouvier, A., Frossard, P., Hammouda, T., Garçon, M., and Gannoun, A.
594 (2018). Enstatite chondrites EL3 as building blocks for the Earth: The debate over
595 the 146 Sm– 142 Nd systematics. Earth and Planetary Science Letters *488*, 68–78.

596 Braukmüller, N., Wombacher, F., Funk, C., and Münker, C. (2019). Earth's volatile
597 element depletion pattern inherited from a carbonaceous chondrite-like source.
598 Nature Geoscience *12*, 564–568.

599 Burbine, T.H., O'Brien, K.M., 2004. Determining the possible building blocks of the
600 Earth and Mars. Meteorit. Planet. Sci. 39, 667–681.

601 Burnham, A.D., Berry, A.J., Halse, H.R., Schofield, P.F., Cibin, G., and Mosselmans,
602 J.F.W. (2015). The oxidation state of europium in silicate melts as a function of

oxygen fugacity, composition and temperature. Chemical Geology *411*, 248–259.

Campbell, I.H., and St C. O'Neill, H. (2012). Evidence against a chondritic Earth. Nature *483*, 553–558.

Cartier, C., Hammouda, T., Boyet, M., Bouhifd, M.A., and Devidal, J.-L. (2014). Redox control of the fractionation of niobium and tantalum during planetary accretion and core formation. Nature Geoscience *7*, 573–576.

Dauphas, N. (2017). The isotopic nature of the Earth's accreting material through time. Nature *541*, 521–524.

Dauphas, N., Chen, J.H., Zhang, J., Papanastassiou, D.A., Davis, A.M., and Travaglio, C. (2014). Calcium-48 isotopic anomalies in bulk chondrites and achondrites: Evidence for a uniform isotopic reservoir in the inner protoplanetary disk. Earth and Planetary Science Letters *407*, 96–108.

Faure, P., Bouhifd, M.A., Boyet, M., Manthilake, G., Clesi, V., and Devidal, J.-L. (2020). Uranium and thorium partitioning in the bulk silicate Earth and the oxygen content of Earth's core. Geochimica et Cosmochimica Acta *275*, 83–98.

Fischer, R.A., Nakajima, Y., Campbell, A.J., Frost, D.J., Harries, D., Langenhorst, F., Miyajima, N., Pollok, K., and Rubie, D.C. (2015). High pressure metal–silicate partitioning of Ni, Co, V, Cr, Si, and O. Geochimica et Cosmochimica Acta *167*, 177–194.

Fitoussi, C., and Bourdon, B. (2012). Silicon Isotope Evidence Against an Enstatite Chondrite Earth. Science *335*, 1477–1480.

Fukao, Y., and Obayashi, M. (2013). Subducted slabs stagnant above, penetrating through, and trapped below the 660 km discontinuity: subducted slabs in the transitions zone. Journal of Geophysical Research: Solid Earth *118*, 5920–5938.

627 Gagnon, J.E., Fryer, B.J., Samson, I.M., and Williams-Jones, A.E. (2008). Quantitative
628 analysis of silicate certified reference materials by LA-ICPMS with and without
629 an internal standard. Journal of Analytical Atomic Spectrometry *23*, 1529.
630 Halliday, A.N. (2004). Mixing, volatile loss and compositional change during impact-
631 driven accretion of the Earth. Nature *427*, 505–509.
632 Hammouda, T. (2003). High-pressure melting of carbonated eclogite and experimental
633 constraints on carbon recycling and storage in the mantle. Earth and Planetary
634 Science Letters *214*, 357–368.
635 Hart, S.R., and Zindler, A. (1986). In search of a bulk-Earth composition. Chemical
636 Geology *57*, 247–267.
637 Hofmann, A. (2014). Sampling Mantle Heterogeneity through Oceanic Basalts: Isotopes
638 and Trace Elements. Treatise on Geochemistry *2*, 67–101.
639 Holzheid, A., Palme, H., and Chakraborty, S. (1997). The activities of NiO, CoO and
640 FeO in silicate melts. Chemical Geology *139*, 21–38.
641 Hubbard, A., and Ebel, D.S. (2014). Protoplanetary dust porosity and FU Orionis
642 outbursts: Solving the mystery of Earth's missing volatiles. Icarus *237*, 84–96.
643 Hyung, E., Huang, S., Petaev, M.I., and Jacobsen, S.B. (2016). Is the mantle chemically
644 stratified? Insights from sound velocity modeling and isotope evolution of an
645 early magma ocean. Earth and Planetary Science Letters *440*, 158–168.
646 Ingrao, N.J., Hammouda, T., Boyet, M., Gaborieau, M., Moine, B.N., Vlastelic, I.,
647 Bouhifd, M.A., Devidal, J.-L., Mathon, O., Testemale, D., et al. (2019). Rare
648 Earth Element Partitioning Between Sulphides and Melt: Evidence for Yb2+ and
649 Sm2+ in EH Chondrites. Geochimica et Cosmochimica Acta.

650 Javoy, M., Kaminski, E., Guyot, F., Andrault, D., Sanloup, C., Moreira, M., Labrosse,
651 S., Jambon, A., Agrinier, P., Davaille, A., Jaupart, C., 2010. The chemical
652 composition of the Earth: enstatite chondrite models. Earth Planet. Sci. Lett. 293
653 (3-4), 259–268.
654 Jellinek, A.M., Jackson, M.G. (2015). Connections between the bulk composition,
655 geodynamics and habitability of Earth. *Nature Geoscience*, *8*(8), 587-593.
656 Li, J., Hadidiacos, C., Mao, H.-K., Fei, Y., and Hemley, R.J. (2003). Behavior of
657 thermocouples under high pressure in a multi-anvil apparatus. High Pressure
658 Research *23*, 389–401.
659 Liebske, C., and Khan, A. (2019). On the principal building blocks of Mars and Earth.
660 Icarus *322*, 121–134.
661 Lodders, K. (1996). An experimental and theoretical study of rare earth element
662 partitioning between sulfides (FeS, CaS) and silicate and application to enstatite
663 achondrites. Meteoritics and Planetary Science *31*, 749–766.
664 Lodders, K. (2000). An Oxygen Isotope Mixing Model for the Accretion and
665 Composition of Rocky Planets. Space Science Reviews *92*, 341–354.
666 Lodders, K. (2003). Solar System Abundances and Condensation Temperatures of the
667 Elements. The Astrophysical Journal *591*, 1220–1247.
668 Lyubetskaya, T., and Korenaga, J. (2007). Chemical composition of Earth's primitive
669 mantle and its variance. Journal of Geophysical Research *112*.
670 Ma, Z. (2001). Thermodynamic description for concentrated metallic solutions using
671 interaction parameters. Metallurgical and Materials Transactions B *32*, 87–103.
672 McDonough, W.F., and Sun, S. -s (1995). The composition of the Earth. Chemical
673 Geology *120*, 223–253.

674 Munker, C. (2003). Evolution of Planetary Cores and the Earth-Moon System from
675 Nb/Ta Systematics. Science *301*, 84–87.
676 Palme, H., and O'Neill, H.St.C. (2014). Cosmochemical Estimates of Mantle
677 Composition. In Treatise on Geochemistry, (Elsevier), 1–39.
678 Righter, K., Pando, K.M., Danielson, L., and Lee, C.-T. (2010). Partitioning of Mo, P
679 and other siderophile elements (Cu, Ga, Sn, Ni, Co, Cr, Mn, V, and W) between
680 metal and silicate melt as a function of temperature and silicate melt composition.
681 Earth and Planetary Science Letters *291*, 1–9.
682 Ringwood, A.E. (1989). Significance of the terrestrial Mg/Si ratio. Earth and Planetary
683 Science Letters *95*, 1–7.
684 Rubin, A.E. (1983). Impact melt-rock clasts in the Hvittis enstatite chondrite breccia-
685 Implications for a genetic relationship between EL chondrites and aubrites. In
686 Lunar and Planetary Science Conference Proceedings, B293–B300.
687 Saji, N.S., Wielandt, D., Paton, C., and Bizzarro, M. (2016). Ultra-high-precision Nd-
688 isotope measurements of geological materials by MC-ICPMS. Journal of
689 Analytical Atomic Spectrometry *31*, 1490–1504.
690 Siebert, J., Corgne, A., and Ryerson, F.J. (2011). Systematics of metal–silicate
691 partitioning for many siderophile elements applied to Earth's core formation.
692 Geochimica et Cosmochimica Acta *75*, 1451–1489.
693 Siebert, J., Sossi, P.A., Blanchard, I., Mahan, B., Badro, J., and Moynier, F. (2018).
694 Chondritic Mn/Na ratio and limited post-nebular volatile loss of the Earth. Earth
695 and Planetary Science Letters *485*, 130–139.
696 Suer, T.-A., Siebert, J., Remusat, L., Menguy, N., Fiquet, G., 2017. A sulfur-poor
697 terrestrial core inferred from metal–silicate partitioning experiments. Earth Planet.

698 Sci. Lett. *469*, 84–97

699 Toplis, M.J. (2004). The thermodynamics of iron and magnesium partitioning between
700 olivine and liquid: criteria for assessing and predicting equilibrium in natural and
701 experimental systems. Contributions to Mineralogy and Petrology *149*, 22–39.

702 Wade, J., and Wood, B.J. (2005). Core formation and the oxidation state of the Earth.
703 Earth and Planetary Science Letters *236*, 78–95.

704 Wang, Z., Laurenz, V., Petitgirard, S., and Becker, H. (2016). Earth's moderately
705 volatile element composition may not be chondritic: Evidence from In, Cd and
706 Zn. Earth and Planetary Science Letters *435*, 136–146.

707 Warren, P.H. (2011). Stable-isotopic anomalies and the accretionary assemblage of the
708 Earth and Mars: A subordinate role for carbonaceous chondrites. Earth and
709 Planetary Science Letters *311*, 93–100.

710 Wasson, J.T., and Kallemeyn, G.W. (1988). Compositions of Chondrites. Philosophical
711 Transactions of the Royal Society A: Mathematical, Physical and Engineering
712 Sciences *325*, 535–544.

713 Wipperfurth, S.A., Guo, M., Šrámek, O., and McDonough, W.F. (2018). Earth's
714 chondritic Th/U: Negligible fractionation during accretion, core formation, and
715 crust–mantle differentiation. Earth and Planetary Science Letters *498*, 196–202.

716 Wohlers, A., and Wood, B.J. (2015). A Mercury-like component of early Earth yields
717 uranium in the core and high mantle ^{142}Nd. Nature *520*, 337–340.

718 Wohlers, A., and Wood, B.J. (2017). Uranium, thorium and REE partitioning into
719 sulfide liquids: Implications for reduced S-rich bodies. Geochimica et
720 Cosmochimica Acta *205*, 226–244.

721 Wood, B.J., and Halliday, A.N. (2005). Cooling of the Earth and core formation after

722 the giant impact. Nature *437*, 1345–1348.
723 Zhang, Z., Stixrude, L., and Brodholt, J. (2013). Elastic properties of MgSiO3-
724 perovskite under lower mantle conditions and the composition of the deep Earth.
725 Earth and Planetary Science Letters *379*, 1–12.
726

727 **Figure Captions**

728

729 **Figure 1**. Backscattered electron image of the sample #1322, recovered from a 6 GPa
730 and 2503 K experiment in a graphite capsule.

731

732 **Figure 2**. Evolution of metal-silicate partition coeffcients for neodymium and europium
733 (D_{Nd} and D_{Eu}) with log fo_2. Datapoints are from this study (Appendix A) and from the
734 litterature (Apprendix B). Data are corrected for the effect of metalic sulfur using the
735 parametrization presented in equation 6 and Table 2. Similar binary plots for other
736 studied REE are given in Appendix D.1. Dashed line represents fitted linear regression,
737 in agreement with equation 6 and parameters values displayed in Table 2.

738

739 **Figure 3.** Evolution of metal-silicate partition coefficients for neodymium and
740 europium (D_{Nd} and D_{Eu}) with the S concentration in the metal. Datapoints are from this
741 study (Appendix A) and from the litterature (Apprendix C). Data are corrected for the
742 effect of oxygen fugacity using the parametrization presented in equation 6 and Table 2.
743 Similar binary plots for other studied REE are given in Appendix D.1. Dashed line
744 represents fitted linear regression, in agreement with equation 6 and parameters values
745 displayed in Table 2.

746

747 **Figure 4**. Sulfur-silicate partition coefficients for REE (normalized to D_{Nd}) determined
748 in all S-rich experiments (Xs from 25.3 to 35.2 wt. %). The average sulfur-silicate
749 partition coefficients from Ingrao et al. (2019), Lodders (1996) and Wohlers and Wood
750 (2017) are also plotted. Error bars are not shown for clarity, but D_{Eu} values are

751 significantly distinct from those of other REE (with the exception of experiment #509
752 and Wohlers and Wood, 2017).
753
754 **Figure 5.** Ratio of metal-silicate partition coefficients determined for Sm and Nd
755 ($D_{Sm}/D_{Nd)}$ as a function of oxygen fugacity. Data presented are from this study as well
756 as those from the literature for experiments performed over the chondritic liquidus.
757 Error bars display the 1σ uncertainties on original data. These samples present S
758 contents in the metallic phase ranging from 0 to 35 wt.%.
759
760 **Figure 6.** RLE enrichment factors of the BSE calculated from accretion scenarios using
761 mixtures of different chondritic building blocks, compared with published BSE
762 composition models. Open circles represent RLE enrichment factors determined from
763 our accretion model in the BSE using measured chondrite compositions. Higher values
764 of RLE enrichment factors (noted EF_{dry} in Table 4) are obtained when the volatile
765 depletion is taken into account. BSE enrichment factors in RLE (EF_{dry}) are well
766 reproduced by BSE composition from McDonough and Sun, (1995) and Palme and
767 O'Neill, (2014).

Table 1. Experimental conditions (P, T, fo_2) and metal-silicate partition coefficients of REE (La to Gd) for the different samples. Given uncertainties are 1 sigma. For this work, different doping solutions were synthesized. Type A solution contained La, Ce, Pr, Nd and Sm, while type B solution contained Nd, Sm, Eu and Gd. For sulphur-rich experiments, a type C solution containing all 7 REE from La to Gd was prepared. *Temperature determined using the power/temperature relation deduced from previous experiments.

Run	Capsule	Doping solution	P (GPa)	T (K)	log fo_2 (ΔIW)	D_{La}	D_{Ce}	D_{Pr}	D_{Nd}	D_{Sm}	D_{Eu}	D_{Gd}
509	Graphite	C	6	2361	-0.60	6.19×10^{-4} $\pm 1.63\times10^{-4}$	1.01×10^{-3} $\pm1.33\times10^{-4}$	9.28×10^{-4} $\pm1.23\times10^{-4}$	9.98×10^{-4} $\pm1.67\times10^{-4}$	9.49×10^{-4} $\pm1.88\times10^{-4}$	1.31×10^{-3} $\pm1.86\times10^{-4}$	7.16×10^{-4} $\pm2.09\times10^{-4}$
536	Graphite	C	6	2386	-0.47	1.40×10^{-3} $\pm8.24\times10^{-5}$	2.35×10^{-3} $\pm3.70\times10^{-4}$	1.98×10^{-3} $\pm1.55\times10^{-4}$	1.86×10^{-3} $\pm5.95\times10^{-5}$	1.49×10^{-3} $\pm1.85\times10^{-4}$	4.95×10^{-3} $\pm3.14\times10^{-4}$	8.33×10^{-4} $\pm5.88\times10^{-5}$
581	Graphite	C	6	2563*	-0.86	4.24×10^{-4} $\pm8.44\times10^{-5}$	5.86×10^{-4} $\pm1.16\times10^{-4}$	5.41×10^{-4} $\pm8.95\times10^{-5}$	4.81×10^{-4} $\pm9.93\times10^{-5}$	3.56×10^{-4} $\pm5.16\times10^{-5}$	1.01×10^{-3} $\pm1.44\times10^{-4}$	2.10×10^{-4} $\pm2.16\times10^{-4}$
594	Graphite	B	6	2388	-3.18				1.76×10^{-4} $\pm1.48\times10^{-5}$	1.40×10^{-4} $\pm1.99\times10^{-5}$	2.19×10^{-4} $\pm1.77\times10^{-5}$	1.00×10^{-4} $\pm6.96\times10^{-6}$
596	Graphite	B	6	2499	-3.40				3.38×10^{-5} $\pm1.04\times10^{-5}$	3.50×10^{-5} $\pm5.11\times10^{-7}$	2.46×10^{-5} $\pm5.02\times10^{-7}$	2.61×10^{-5} $\pm9.61\times10^{-7}$
598	Graphite	A	6	2543	-1.47	1.92×10^{-5} $\pm4.96\times10^{-6}$	1.79×10^{-5} $\pm1.71\times10^{-6}$	1.11×10^{-5} $\pm4.01\times10^{-6}$	1.10×10^{-5} $\pm1.77\times10^{-6}$	1.07×10^{-5} $\pm1.55\times10^{-6}$		
599	Graphite	A	6	2532	-3.26	5.99×10^{-5} $\pm2.89\times10^{-5}$	8.24×10^{-5} $\pm1.42\times10^{-6}$	5.97×10^{-5} $\pm3.95\times10^{-6}$	6.76×10^{-5} $\pm5.17\times10^{-6}$	7.22×10^{-5} $\pm1.66\times10^{-5}$		
600	Graphite	A	6	2536	-2.81	1.25×10^{-5} $\pm9.85\times10^{-6}$	2.22×10^{-5} $\pm9.56\times10^{-6}$	1.39×10^{-5} $\pm3.47\times10^{-6}$	2.09×10^{-5} $\pm4.65\times10^{-6}$	1.94×10^{-5} $\pm1.53\times10^{-6}$		
601	Graphite	A	6	2517	-3.58	2.19×10^{-5} $\pm1.44\times10^{-5}$	4.87×10^{-5} $\pm1.82\times10^{-5}$	4.40×10^{-5} $\pm1.23\times10^{-5}$	5.00×10^{-5} $\pm1.70\times10^{-5}$	6.96×10^{-5} $\pm1.43\times10^{-5}$		
603	Graphite	B	6	2500	-3.48				2.66×10^{-5} $\pm4.41\times10^{-6}$	2.62×10^{-5} $\pm2.69\times10^{-6}$	2.21×10^{-5} $\pm3.12\times10^{-6}$	1.61×10^{-5} $\pm2.22\times10^{-6}$
685	Graphite	C	6	2529*	-0.68	1.02×10^{-3} $\pm3.73\times10^{-4}$	1.42×10^{-3} $\pm5.23\times10^{-4}$	1.33×10^{-3} $\pm4.68\times10^{-4}$	1.21×10^{-3} $\pm4.54\times10^{-4}$	1.02×10^{-3} $\pm4.01\times10^{-4}$	2.30×10^{-3} $\pm7.54\times10^{-4}$	6.40×10^{-4} $\pm2.70\times10^{-4}$
693	MgO single crystal	B	14	2560	-1.51				1.25×10^{-5} $\pm5.70\times10^{-6}$	1.18×10^{-5} $\pm2.64\times10^{-6}$	1.34×10^{-5} $\pm5.31\times10^{-6}$	8.47×10-06 $\pm3.43\times10^{-6}$
694	Graphite	B	6	2365	-0.59				1.83×10^{-5} $\pm2.35\times10^{-6}$	1.77×10^{-5} $\pm2.22\times10^{-6}$	1.29×10^{-5} $\pm6.03\times10^{-6}$	4.59×10^{-5} $\pm3.79\times10^{-5}$
696	MgO single crystal	A	14	2560*	-1.51	2.61×10^{-6} $\pm1.26\times10^{-6}$	6.30×10^{-6} $\pm2.91\times10^{-6}$	4.88×10^{-6} $\pm2.17\times10^{-6}$	5.36×10^{-6} $\pm1.84\times10^{-6}$	6.17×10^{-6} $\pm2.57\times10^{-6}$		
698	Graphite	C	6	2429	-0.63	2.74×10^{-3} $\pm5.05\times10^{-4}$	3.44×10^{-3} $\pm5.44\times10^{-4}$	3.24×10^{-3} $\pm4.87\times10^{-4}$	3.04×10^{-3} $\pm3.76\times10^{-4}$	2.74×10^{-3} $\pm3.12\times10^{-4}$	5.21×10^{-3} $\pm6.54\times10^{-4}$	2.06×10^{-3} $\pm2.80\times10^{-4}$
699	Graphite	C	6	2439	-0.20	4.01×10^{-3} $\pm3.42\times10^{-4}$	4.85×10^{-3} $\pm4.24\times10^{-4}$	4.93×10^{-3} $\pm4.49\times10^{-4}$	4.46×10^{-3} $\pm3.34\times10^{-4}$	4.15×10^{-3} $\pm3.69\times10^{-4}$	7.75×10^{-3} $\pm1.28\times10^{-3}$	3.27×10^{-3} $\pm4.72\times10^{-4}$
1320	Graphite	A	6	2450	-1.38	8.09×10^{-5} $\pm1.12\times10^{-4}$	1.89×10^{-5} $\pm9.66\times10^{-6}$	1.31×10^{-5} $\pm3.09\times10^{-6}$	9.36×10^{-6} $\pm1.85\times10^{-6}$	2.31×10^{-5} $\pm3.75\times10^{-6}$		
1321	Graphite	A	6	2543*	-2.67	1.56×10^{-4} $\pm4.82\times10^{-6}$	2.21×10^{-4} $\pm7.30\times10^{-6}$	2.24×10^{-4} $\pm8.93\times10^{-6}$	2.29×10^{-4} $\pm1.25\times10^{-5}$	2.98×10^{-4} $\pm1.47\times10^{-5}$		
1322	Graphite	A	6	2486*	-3.16	1.71×10^{-4} $\pm3.98\times10^{-6}$	3.10×10^{-4} $\pm3.33\times10^{-6}$	3.26×10^{-4} $\pm4.45\times10^{-6}$	3.54×10^{-4} $\pm5.58\times10^{-6}$	4.70×10^{-4} $\pm9.25\times10^{-6}$		
1323	Graphite	A	6	2503	-3.42	3.27×10^{-4} $\pm1.15\times10^{-4}$	5.11×10^{-4} $\pm1.09\times10^{-4}$	6.04×10^{-4} $\pm1.03\times10^{-4}$	6.55×10^{-4} $\pm8.62\times10^{-5}$	7.65×10^{-4} $\pm1.22\times10^{-4}$		
1324	Graphite	B	6	2499*	-0.82				4.86×10^{-5} $\pm3.71\times10^{-5}$	7.60×10^{-5} $\pm4.17\times10^{-5}$	7.45×10^{-5} $\pm5.94\times10^{-5}$	6.97×10^{-5} $\pm2.12\times10^{-5}$
1325	Graphite	B	6	2517	-3.11				2.80×10^{-5} $\pm9.16\times10^{-6}$	4.42×10^{-5} $\pm1.22\times10^{-5}$	5.54×10^{-5} $\pm1.07\times10^{-5}$	4.34×10^{-5} $\pm3.68\times10^{-5}$
1326	Graphite	B	6	2536	-3.95				1.10×10^{-3} $\pm5.73\times10^{-5}$	1.37×10^{-3} $\pm1.12\times10^{-4}$	8.30×10^{-4} $\pm5.95\times10^{-5}$	1.02×10^{-3} $\pm1.37\times10^{-4}$
1327	Graphite	B	6	2519	-3.46				1.88×10^{-4} $\pm1.73\times10^{-4}$	2.96×10^{-4} $\pm1.51\times10^{-4}$	1.71×10^{-4} $\pm1.27\times10^{-4}$	3.21×10^{-4} $\pm4.06\times10^{-6}$

Table 2. Results of the multi-variable linear regression based on Equation 6 using experimental data from this study and those from literature listed in Appendix B. Two-variable parametrizations regressed the variables related to log fO_2 (*a*), the metallic concentration of S (*d*), along with the equation constant (e). The p-value for each variable used is also shown, with a significance level of 5%.

Element	***N°***	***R^2***	***a***	*p-value*	***d***	*p-value*	***e***	*p-value*
La	25	**0.86**	-0.61 ±0.12	$1.90 .10^{-5}$	-14.20 ±1.5	$3.41 .10^{-9}$	-5.34 ±0.27	$2.90 .10^{-15}$
Ce	24	**0.87**	-0.60 ±0.10	$6.66 .10^{-5}$	-13.45 ±1.40	$4.23 .10^{-9}$	-5.23 ±0.26	$4.37 .10^{-15}$
Pr	21	**0.88**	-0.61 ±0.08	$6.50 .10^{-5}$	-12.65 ±1.30	$1.31 .10^{-8}$	-5.24 ±0.23	$1.63 .10^{-14}$
Nd	42	**0.81**	-0.62 ±0.09	$7.00 .10^{-8}$	-12.45 ±1.16	$2.47 .10^{-13}$	-5.19 ±0.21	$5.17 .10^{-26}$
Sm	42	**0.8**	-0.61 ±0.08	$5.14 .10^{-8}$	-11.91 ±1.17	$1.01 .10^{-12}$	-5.13 ±0.21	$9.24 .10^{-26}$
Eu	25	**0.9**	-0.40 ±0.11	$9.64 .10^{-5}$	-15.12 ±1.24	$3.02 .10^{-11}$	-5.10 ±0.23	$1.30 .10^{-16}$
Gd	20	**0.89**	-0.63 ±0.14	$3.82 .10^{-5}$	-11.59 ±1.17	$1.07 .10^{-8}$	-5.24 ±0.21	$2.43 .10^{-15}$

Table 3. Concentration of REE (La to Gd), in ppb, along with the enrichment factor (EF) in RLE compared to CI for the BSE proposed in the literature, based on cosmochemichal and/or petrological approaches. All EF are taken from the original papers, with the exception of Allègre et al. (2001), for which the EF is calculated using REE concentrations in the BSE normalized to CI chondrite concentrations given by Barrat et al. (2012). Uncertainties on EF presented here are taken from the original papers for Palme and O'Neill (2014) and Lyubetskaya and Korenaga (2007), and extrapolated from the uncertainties on the REE concentrations given in the BSE in Allègre et al. (2001) and McDonough and Sun (1995). Uncertainty (1σ) on the enrichment factor takes into account the uncertainties on the BSE and the CI compositions.

	La	**Ce**	**Pr**	**Nd**	**Sm**	**Eu**	**Gd**	**EF compared to CI**
Palme and O'Neill, 2014	683 ±68	1753 ±175	265 ±39	1341 ±134	434 ±43	166 ±17	585 ±29	**2.83 ± 0.23**
Lyubetskaya and Korenaga, 2007	508 ±87	1340 ±230	203 ±35	994 ±170	324 ±55	123 ±21	432 ±74	**2.16 ± 0.37**
Allègre et al., 2001	415 ±42	1088 ±218	165 ±8	814 ±81	259 ±8	97.9 ±3	348 ±28	**1.70 ± 0.24**
McDonough and Sun, 1995	648 ±65	1675 ±168	254 ±25	1250 ±125	406 ±41	154 ±15	544 ±54	**2.75 ± 0.27**

Table 4. Presentation of the accretion models considered in this study. a) Building block mixing proposed by several authors (in %) in order to create the BSE nucleosynthetic composition, which also reproduce several elemental ratios of the BSE (see text for details). b) Resulting REE concentrations (ppb) in the BSE, along with their 1 sigma uncertainty. Where no precision relative to the chondritic subgroup is given, an average concentration of every subgroup is used to define the building block compositions. Concentrations used for chondrites are reported in Appendix E. Two enrichment factors based on these REE concentrations are reported for each model. EF is obtained using the measured composition of chondrites, whereas EF_{dry} is based on chondritic compositions depleted in volatile elements to match the terrestrial depletion (see text for more details). The resulting enrichment factors are calculated for each REE based on the composition of CI chondrite given by Barrat et al. (2012). Uncertainty (1σ) on the enrichment factor takes into account the uncertainties on the calculated BSE and the CI composition.

a)	**Enstatite Chondrites**		**Carbonaceous Chondrites**				**Ordinary Chondrites**		
	EH	**EL**	**CI**	**CV**	**CO**	**CM**	**H**	**L**	**LL**
Dauphas, 2017	**71**				**24**		**5**		
Dauphas et al., 2014	**91**		**2**				**7**		
Warren, 2011	**76**		**24**						
Lodders, 2000	**70**		**4**	**5**			**21**		

b)	**Resulting BSE composition**							EF	**EF_{dry}**
	La	*Ce*	*Pr*	*Nd*	*Sm*	*Eu*	*Gd*		
Dauphas et al., 2017	442 ±31	1156 ±69	179 ±11	919 ±74	299 ±27	108 ±10	423 ±38	1.80± 0.24	2.94± 0.24
Dauphas et al., 2014	405 ±36	1061 ±85	162 ±11	829 ±50	270 ±16	96 ±8	380 ±30	1.65 ± 0.26	2.69± 0.26
Warren et al., 2011	402 ±32	1047 ±73	160 ±10	814 ±58	262 ±24	98 ±6	369 ±30	1.76± 0.23	2.87± 0.23
Lodders, 2000	425 ±30	1074 ±86	162 ±11	807 ±57	255 ±18	95 ±8	352 ±32	1.86± 0.24	3.05± 0.24

Figure 1 .

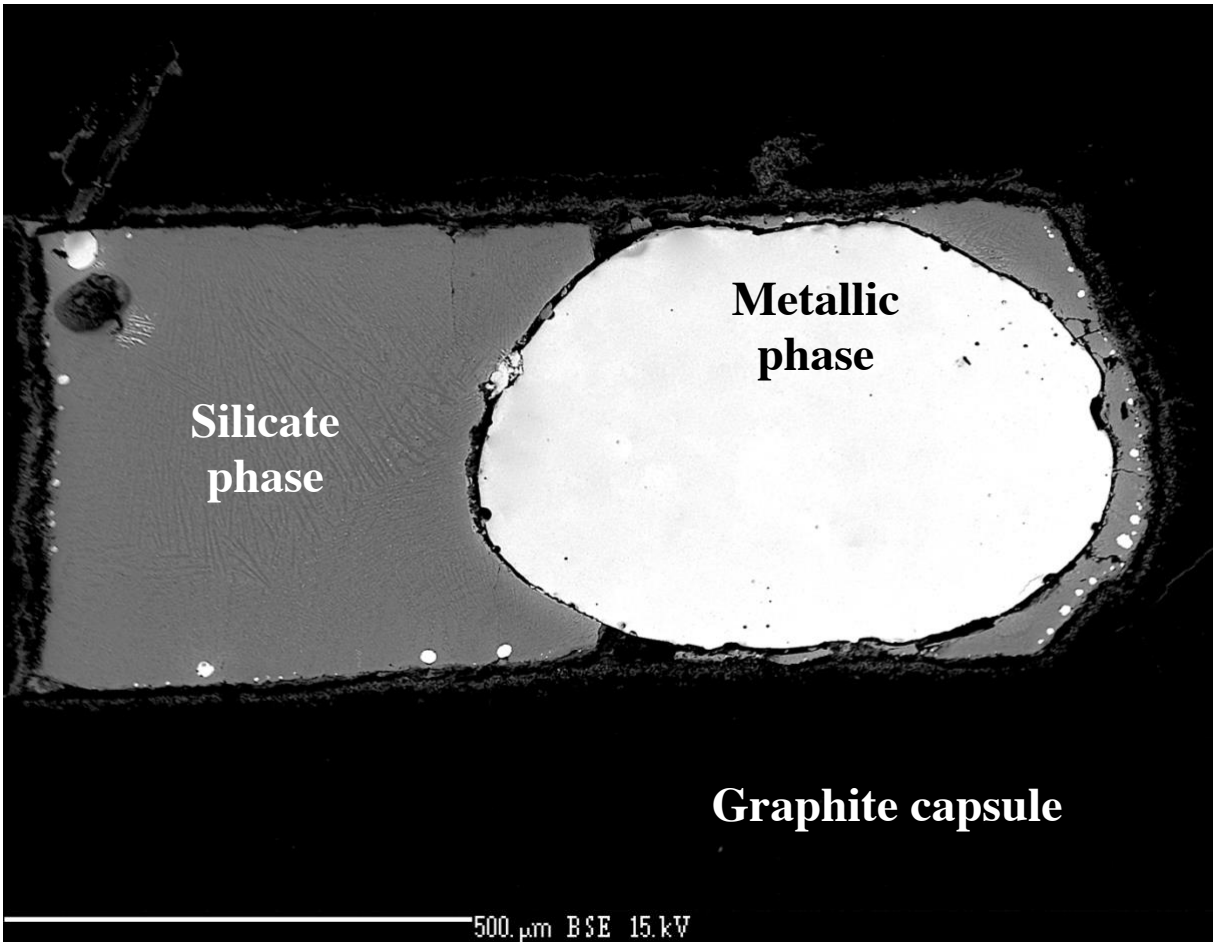
Metallic
phase
Silicate
phase
Graphite capsule
500.μm BSE 15.kV

Figure 2 .

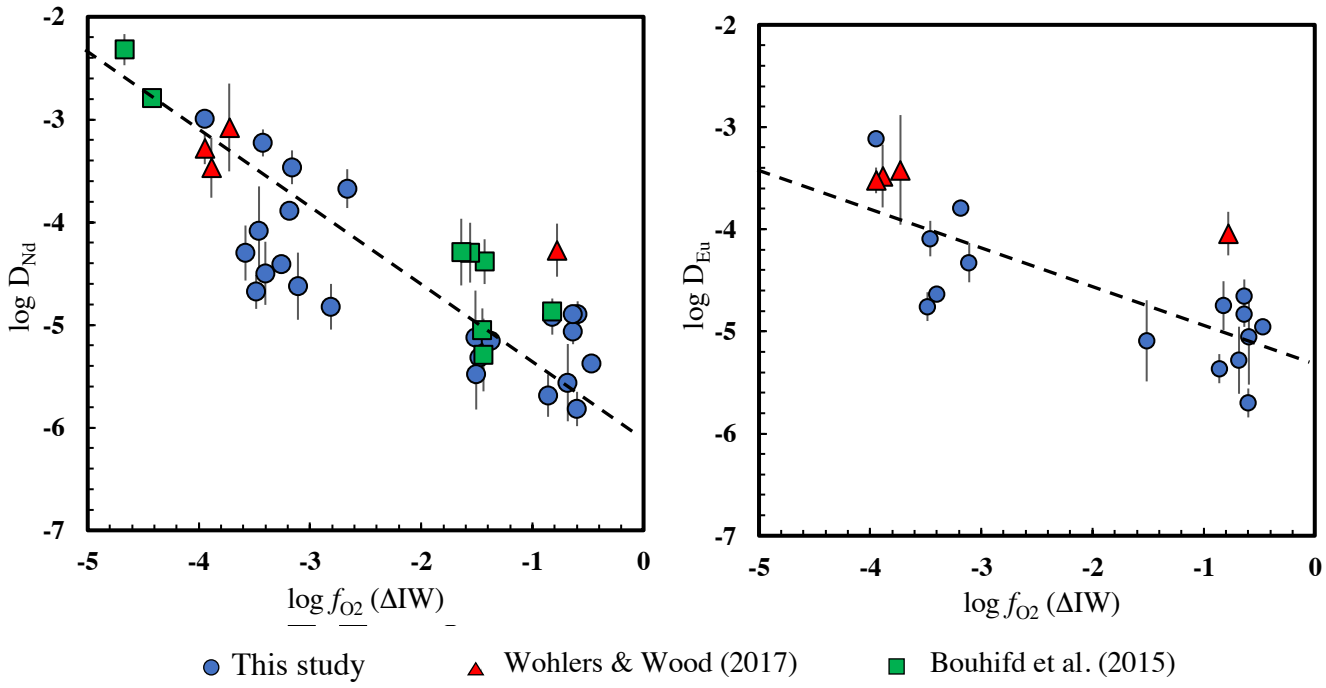
log D_{Nd}
log D_{Eu}
log f_{O2} (ΔIW)
log f_{O2} (ΔIW)
This study
Wohlers & Wood (2017)
Bouhifd et al. (2015)

Figure 3.

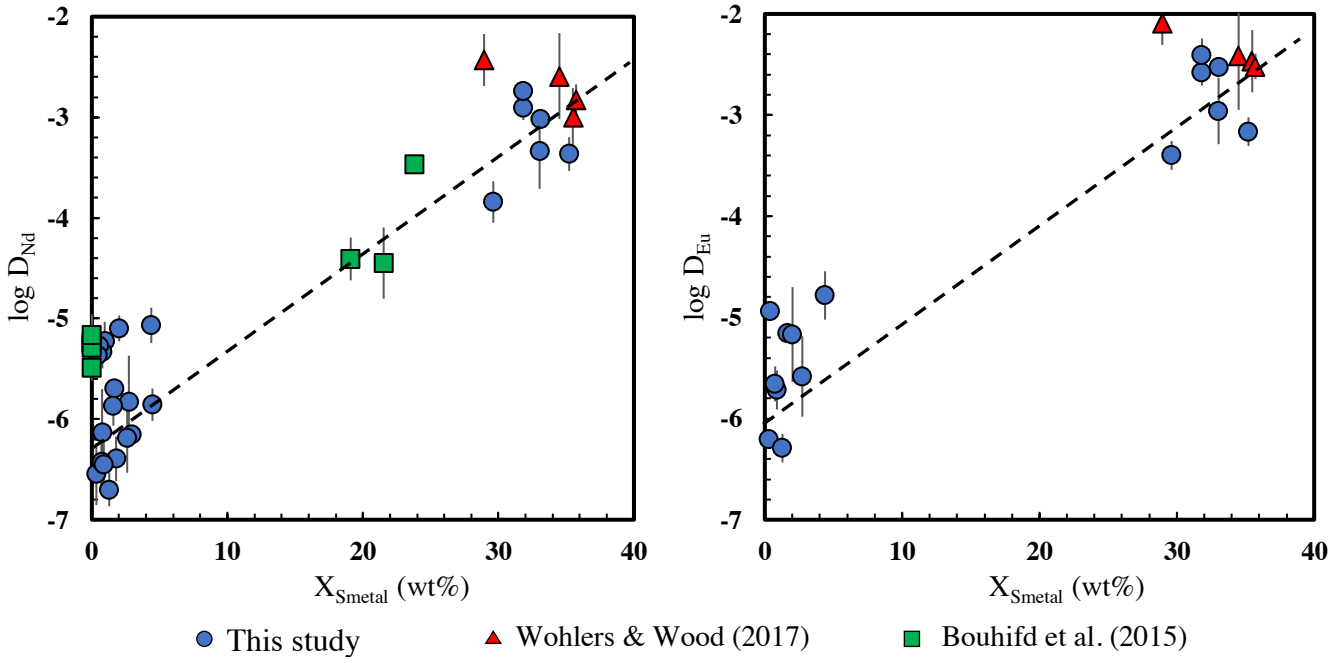
-2
-3
-4
-5
-6
-7
log D_{Nd}
0
10
20
30
40
X_{Smetal} (wt%)
log D_{Eu}
This study
Wohlers & Wood (2017)
Bouhifd et al. (2015)

Figure 4.

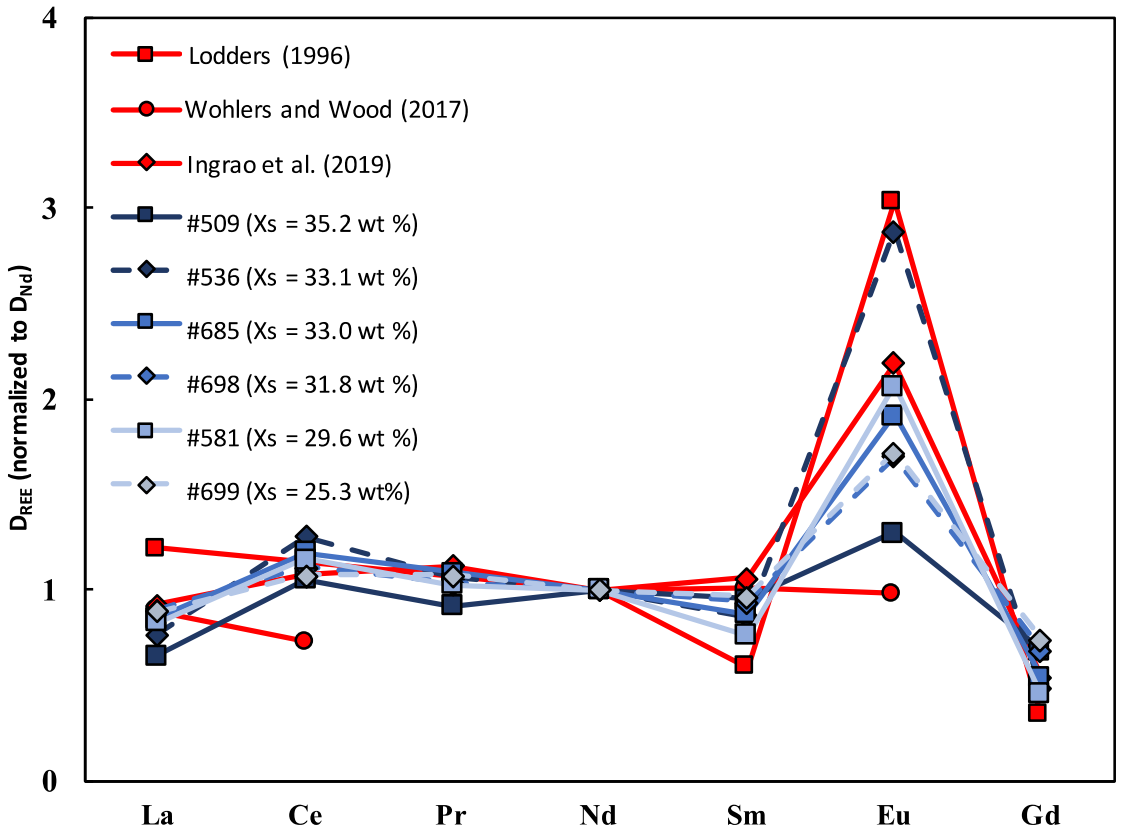
Lodders (1996)
Wohlers and Wood (2017)
Ingrao et al. (2019)
#509 (Xs = 35.2 wt %)
#536 (Xs = 33.1 wt %)
#685 (Xs = 33.0 wt %)
#698 (Xs = 31.8 wt %)
#581 (Xs = 29.6 wt %)
#699 (Xs = 25.3 wt%)
D_REE (normalized to D_Nd)
0
1
2
3
4
La
Ce
Pr
Nd
Sm
Eu
Gd

Figure 5.

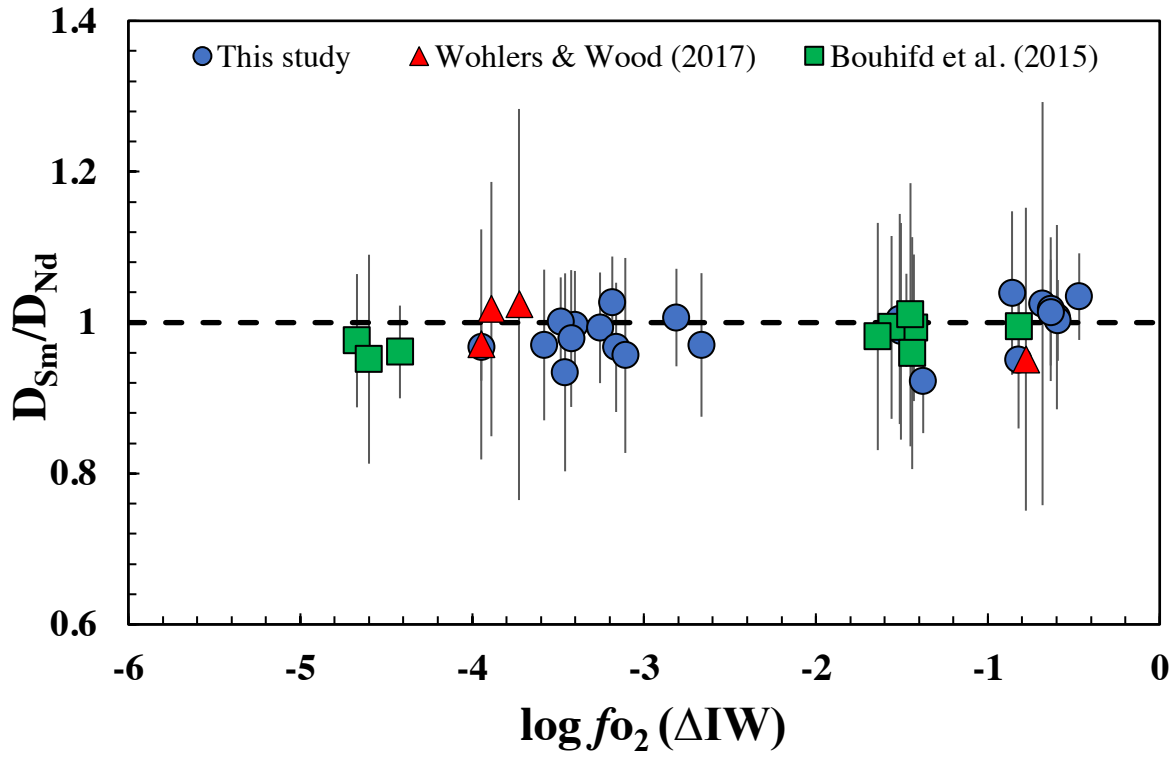
This study
Wohlers & Wood (2017)
Bouhifd et al. (2015)
1.4
1.2
1
0.8
0.6
D_{Sm}/D_{Nd}
-6
-5
-4
-3
-2
-1
0
log fo_2 (ΔIW)

Figure 6.

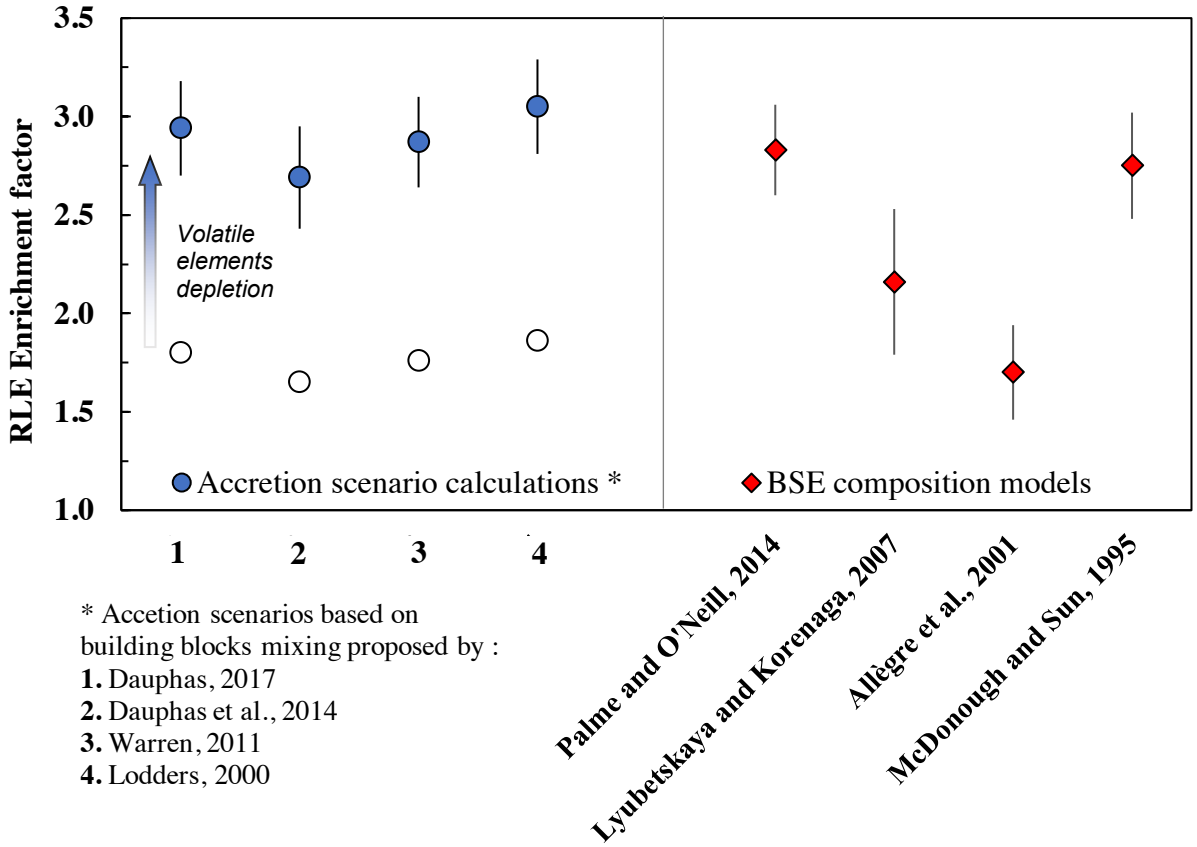

* Accetion scenarios based on building blocks mixing proposed by :

1. Dauphas, 2017
2. Dauphas et al., 2014
3. Warren, 2011
4. Lodders, 2000

Appendix A1. Chemical analysis of all run products

Run	**509**	**536**	**581**	**594**	**596**	**598**	**599**	**600**	**601**	**603**	**685**	**693**	**694**	**696**	**698**	**699**	**1320**	**1321**	**1322**	**1323**	**1324**	**1325**	**1326**	**1327**
Capsule	Gr	Gr	Gr	Gr	Gr	Gr	Gr	Gr	Gr	Gr	Gr	MgO	Gr	MgO	Gr	Gr	Gr	Gr	Gr	Gr	Gr	Gr	Gr	Gr
P (GPa)	6	6	6	6	6	6	6	6	6	6	6	14	6	14	6	6	6	6	6	6	6	6	6	6
T (K)	2361	2386	2563	2388	2499	2543	2532	2536	2517	2500	2529	2560	2365	2560	2429	2439	2450	2543	2486	2503	2499	2517	2536	2519
NBO/T	2.19	2.07	2.29	1.21	1.46	1.81	1.56	1.42	1.26	1.20	1.34	3.66	2.28	3.66	2.41	2.78	1.93	1.81	1.77	1.46	1.46	1.26	1.42	1.69
Doping solution	C	C	C	B	B	A	A	A	A	B	C	B	B	A	C	C	A	A	A	A	B	B	B	B
Silicate major elements (wt%)																								
SiO_2	43.15 ±0.81	38.59 ±2.94	44.83 ±4.01	64.22 ±0.53	65.66 ±0.73	55.91 ±0.37	62.52 ±0.44	66.54 ±0.34	64.42 ±0.65	63.72 ±0.84	46.31 ±1.19	40.50 ±0.76	46.33 ±0.52	40.73 ±0.93	45.95 ±1.44	39.77 ±0.54	55.24 ±0.67	62.45 ±0.54	58.28 ±1.32	63.06 ±0.47	50.13 ±0.61	64.58 ±0.4	64.93 ±0.52	62.22 ±0.27
Al_2O_3	2.10 ±0.06	1.63 ±0.78	3.08 ±1.80	4.93 ±0.09	2.84 ±0.07	2.30 ±0.07	2.23 ±0.08	2.32 ±0.11	2.37 ±0.23	2.56 ±0.20	2.02 ±0.05	0.69 ±0.25	2. 01 ±0.09	0.86 ±0.23	2.05 ±0.23	1.93 ±0.09	1.8 ±0.15	2.02 ±0.05	4.07 ±0.86	2.07 ±0.06	2.12 ±0.08	2.55 ±0.05	2.61 ±0.05	1.84 ±0.02
FeO	29.60 ±0.62	33.79 ±5.14	24.20 ±3.61	0.93 ±0.60	0.43 ±0.36	6.05 ±0.30	0.89 ±0.13	1.31 ±0.68	0.41 ±0.12	0.64 ±0.08	21.16 ±1.62	7.77 ±0.57	20.39 ±0.6	7.92 ±0.77	22.98 ±1.89	31.25 ±0.63	8.08 ±0.8	1.77 ±0.85	0.96 ±0.33	0.60 ±0.34	13.60 ±0.93	1.03 ±0.1	0.28 ±0.12	0.59 ±0.1
MnO	0.14 ±0.01	0.20 ±0.06	0.19 ±0.01	0.17 ±0.03	0.06 ±0.04	0.27 ±0.02	0.12 ±0.01	0.06 ±0.02	0.09 ±0.04	0.04 ±0.04	0.18 ±0.02	0.04 ±0.02	0.12 ±0.03	0.01 ±0.01	0.18 ±0.03	0.16 ±0.02	0.10 ±0.03	0.02 ±0.02	0.03 ±0.01	0.03 ±0.02	0.08 ±0.05	0.02 ±0.02	0.04 ±0.03	0.06 ±0.03
MgO	23.82 ±0.61	24.27 ±1.92	20.89 ±6.35	23.89 ±0.32	31.11 ±0.68	30.22 ±0.46	31.52 ±0.44	25.92 ±1.75	31.46 ±1.87	24.16 ±2.02	24.59 ±0.48	45.67 ±2.04	23.87 ±0.32	45.37 ±1.84	23.78 ±0.52	19.99 ±0.65	30.93 ±1.01	29.08 ±0.15	34.37 ±0.34	29.62 ±0.34	27.77 ±0.17	25.67 ±0.4	29.47 ±0.34	34.3 ±0.20
CaO	1.18 ±0.11	1.40 ±0.69	2.20 ±1.94	2.85 ±0.09	1.71 ±0.14	1.63 ±0.06	1.74 ±0.08	1.31 ±0.3	1.35 ±0.14	1.97 ±0.17	1.46 ±0.19	1.02 ±0.45	1.55 ±0.09	1.51 ±0.58	1.60 ±0.25	1.28 ±0.11	1.37 ±0.11	1.59 ±0.04	1.19 ±0.08	1.68 ±0.05	1.74 ±0.08	1.87 ±0.02	2.35 ±0.12	1.44 ±0.07
NiO	0.01 ±0.01	0.13 ±0.07	0.03 ±0.04	0.05 ±0.03	0.01 ±0.02	0.11 ±0.09	0 ±0	0.03 ±0.04	0.01 ±0.01	0.10 ±0.04	0.02 ±0.02	0.12 ±0.02	0.05 ±0.03	0.11 ±0.03	0.03 ±0.04	0.02 ±0.03	0.03 ±0.03	0.00 ±0.00	0.01 ±0.02	0.00 ±0.00	0.09 ±0.02	0.06 ±0.02	0.03 ±0.02	0.01 ±0.01
S	0,44 ±0,17	0,41 ±0,42	0,39 ±0,34	0,85 ±0,02	2,35 ±0,18	0,09 ±0,01	0,58 ±0,05	0,69 ±0,09	1,88 ±0,35	0,52 ±0,12	0,58 ±0,23	0,02 ±0,02	0,06 ±0,02	0,04 ±0,03	0,46 ±0,10	0,32 ±0,04	0,12 ±0,03	0,58 ±0,03	0,40 ±0,04	0,69 ±0,01	0,08 ±0,02	0,91 ±0,04	1,74 ±0,07	0,82 ±0,04
Total	100 ±0.41	100 ±0.25	95.41 ±3.60	97.05 ±0.23	101.81 ±0.58	96.48 ±0.60	99.02 ±0.96	97.49 ±0.96	100.1 ±0.56	93.21 ±1.57	95.75 ±1.11	95.81 ±1.17	94.32 ±0.23	96.51 ±0.7	95.87 ±0.76	94.98 ±0.62	97.55 ±0.86	96.94 ±0.39	98.92 ±0.93	97.06 ±0.82	95.53 ±0.49	95.79 ±0.63	99.71 ±0.85	100.5 ±0.28
Silicate trace elements (ppm)																								
La	1488.76 ±162.88	1115.2 ±15.96	2210.36 ±160.5	n.d.	n.d.	1683.49 ±59.41	1773.03 ±11.19	1825.08 ±120.95	904.13 ±56.85	n.d.	1432.74 ±52.85	n.d.	n.d.	5573.63 ±703.63	1438.02 ±60.84	1440.28 ±60.84	2950.63 ±382.65	4099 ±126.62	1728.8 ±40.32	3501.33 ±42.93	n.d.	n.d.	n.d.	n.d.
Ce	1466.95 ±158.71	1116.8 ±32.4	2241.21 ±134.72	n.d.	n.d.	1935.38 ±64.47	1817.6 ±14.27	1922.86 ±158.84	960.16 ±68.11	n.d.	1442.32 ±34.31	n.d.	n.d.	5000.36 ±569.46	1438.83 ±69	1440.22 ±69	3207.3 ±437.94	4060.12 ±133.97	1847.67 ±19.85	3590.89 ±29.12	n.d.	n.d.	n.d.	n.d.
Pr	1380.46 ±152.28	1092.65 ±8.24	2142.67 ±133.15	n.d.	n.d.	1969.17 ±94.86	1818.56 ±16.18	1885.15 ±134.56	951.79 ±78.97	n.d.	1400.6 ±29.99	n.d.	n.d.	5023.98 ±488.6	1413.92 ±72.87	1410.02 ±72.87	3106.54 ±435.34	3912.61 ±155.66	1824.01 ±24.87	3486.91 ±17.36	n.d.	n.d.	n.d.	n.d.
Nd	1397.98 ±162.8	1106.2 ±1.24	2341.73 ±129.97	4846.55 ±167.12	1306.93 ±12.94	1939.57 ±31.71	1778.71 ±16.68	1883.78 ±138	946.77 ±71.77	11009.18 ±529.81	1414.77 ±35.77	4097.52 ±319.91	6795.43 ±70.15	5190.93 ±494.6	1456.72 ±66.23	1459.12 ±66.23	3171.43 ±476.81	4157.83 ±227.23	1803.75 ±28.45	3662.92 ±12.08	5352.93 ±481.7	8585.13 ±85.86	3676.36 ±37.35	543.56 ±5.34
Sm	1398.14 ±169.83	1180.27 ±20.09	2423.93 ±137.62	5176.65 ±136.5	1377.22 ±12.02	2386.39 ±29.39	1811.96 ±3.45	1976.1 ±147.96	1006.88 ±75.83	10715.86 ±584.18	1466.95 ±28.22	4246.38 ±196.01	6734.14 ±43.76	5368.81 ±422.37	1505.86 ±65.63	1503.46 ±65.63	3598.06 ±466.16	3999.4 ±197.66	1840.75 ±36.19	3700.39 ±7.89	5416.94 ±447.91	8424.43 ±54.29	3858.79 ±31.17	578.14 ±3.3
Eu	1385.91 ±162.88	1193.66 ±16.81	2310.67 ±146.24	5243.2 ±106.64	1404.41 ±11.38	n.d.	n.d.	n.d.	n.d.	9923.99 ±390.9	1428.49 ±25.6	4074.99 ±232.15	6628.3 ±136.34	n.d.	1441.67 ±57.45	1439.66 ±57.45	n.d.	n.d.	n.d.	n.d.	5086.39 ±164.41	7756.16 ±65.18	4041.3 ±42.66	587.45 ±5.23
Gd	1342.66 ±157.84	1183.04 ±2.91	2409.34 ±109.5	5283.7 ±126.88	1375.12 ±10.02	n.d.	n.d.	n.d.	n.d.	10643.77 ±587.79	1460.09 ±33.86	3976.81 ±238.12	6550.85 ±68.65	n.d.	1469.82 ±69.6	1472.12 ±69.6	n.d.	n.d.	n.d.	n.d.	5418.7 ±438.92	8404.09 ±65.13	3976.29 ±26.77	585.48 ±7.41

Appendix A1. (continued)

Run	509	536	581	594	596	598	599	600	601	603	685	693	694	696	698	699	1320	1321	1322	1323	1324	1325	1326	1327
Metal Major elements (wt%)																								
Fe	61.48 ±0.51	61.97 ±0.23	63.13 ±0.51	87.04 ±0.42	75.98 ±0.49	76.09 ±0.85	86.63 ±1.49	84.87 ±0.56	78.47 ±0.31	87.92 ±0.46	61.73 ±0.3	79.11 ±0.74	91.4 ±0.26	79.5 ±0.75	62.75 ±0.22	67.94 ±1.62	83.97 ±0.35	88.28 ±0.33	85.25 ±0.38	82.93 ±0.31	77.89 ±0.78	88.88 ±0.97	80.39 ±0.24	81.64 ±0.27
Ni	1.26 ±0.09	1.47 ±0.1	2.84 ±0.37	1.5 ±0.05	1.12 ±0.08	14.09 ±0.28	2.3 ±0.11	2.18 ±0.1	1.79 ±0.05	1.7 ±0.05	1.79 ±0.05	15.1 ±0.43	1.47 ±0.05	14.83 ±0.25	2.24 ±0.76	4.46 ±1.34	9.41 ±0.24	1.73 ±0.08	4.13 ±0.13	2.8 ±0.07	14.07 ±1.32	0.68 ±0.04	0.72 ±0.05	3.92 ±0.06
S	35.22 ±1.75	33.09 ±0.16	29.62 ±1.39	1.65 ±0.05	0.33 ±0.07	4.47 ±0.26	2.95 ±1.78	1.79 ±0.77	0.7 ±0.35	1.28 ±0.41	33.04 ±0.51	2.73 ±0.27	2.02 ±0.18	2.61 ±0.62	31.83 ±1.09	25.3 ±2.23	1.59 ±0.15	0.95 ±0.06	0.77 ±0.03	0.55 ±0.06	4.38 ±1.23	0.88 ±0.22	0.43 ±0.1	0.76 ±0.16
Si	0.05 ±0.03	0.01 ±0	0.03 ±0.01	6.6 ±0.1	22.52 ±0.46	0.03 ±0.02	4.82 ±0.24	8.76 ±0.21	18.69 ±0.06	5.62 ±0.09	0.08 ±0.04	0.05 ±0.01	0.07 ±0.01	0.03 ±0.01	0.06 ±0.02	0.1 ±0.03	0.11 ±0.03	6.46 ±0.12	7.35 ±0.37	12.92 ±0.13	0.02 ±0.01	6.82 ±0.1	16.65 ±0.63	12.4 ±0.34
Cr	0.09 ±0.01	0.11 ±0.01	0.04 ±0.03	0.16 ±0.01	0.13 ±0.01	0.15 ±0.02	0.21 ±0.09	0.15 ±0.05	0.14 ±0.04	0.13 ±0.02	0.13 ±0.02	0.02 ±0.02	0.05 ±0.02	0.04 ±0.06	0.08 ±0.02	0.02 ±0.01	0.12 ±0.01	0.1 ±0.01	0.06 ±0.01	0.07 ±0.01	0.04 ±0.01	0.12 ±0.04	0.08 ±0.01	0.09 ±0.02
Mn	0.02 ±0	0.04 ±0.01	0.02 ±0.01	0 ±0.01	0 ±0	0 ±0	0 ±0	0 ±0	0 ±0	0 ±0	0 ±0	0 ±0	0 ±0	0 ±0	0 ±0	0 ±0	0 ±0	0 ±0	0 ±0	0 ±0	0 ±0	0 ±0	0 ±0	0 ±0
Total	98,04	96,69	95,67	96,95	99,94	94,82	96,91	97,76	99,79	96,66	96,79	97.01	95,01	97,04	96,97	97,82	95,19	97,52	97,57	99,28	96,41	97,39	98,28	98,8
C*	1.96 ±1.36	3.31 ±0.39	4.33 ±0	3.05 ±0.01	0.06 ±0.13	5.18 ±0.63	3.09 ±0.21	2.24 ±0.3	0.21 ±0.06	3.34 ±0.25	3.21 ±0.48		4.99 ±0.28		3.03 ±0.39	2.18 ±0.35	4.81 ±0.11	2.48 ±0.3	2.43 ±0.22	0.72 ±0.34	3.59 ±0.32	2.61 ±0.85	1.72 ±0.63	1.2 ±0.38
Metal trace elements (ppm)																								
La	0.92 ±0.14	1.57 ±0.07	0.94 ±0.12	n.d.	n.d.	0.03 ±0.01	0.11 ±0.05	0.02 ±0.02	0.02 ±0.01	n.d.	1.46 ±0.48	n.d.	n.d.	0.01 ±0.01	3.95 ±0.56	5.77 ±0.25	0.24 ±0.3	0.64 ±0	0.3 ±0	1.15 ±0.39	n.d.	n.d.	n.d.	n.d.
Ce	1.48 ±0.03	2.62 ±0.34	1.31 ±0.18	n.d.	n.d.	0.03 ±0	0.15 ±0	0.04 ±0.01	0.05 ±0.01	n.d.	2.04 ±0.71	n.d.	n.d.	0.03 ±0.01	4.96 ±0.54	6.98 ±0.28	0.06 ±0.02	0.9 ±0	0.57 ±0	1.84 ±0.38	n.d.	n.d.	n.d.	n.d.
Pr	1.28 ±0.03	2.17 ±0.15	1.16 ±0.12	n.d.	n.d.	0.02 ±0.01	0.11 ±0.01	0.03 ±0	0.04 ±0.01	n.d.	1.86 ±0.62	n.d.	n.d.	0.02 ±0.01	4.58 ±0.45	6.97 ±0.28	0.04 ±0	0.88 ±0	0.6 ±0	2.11 ±0.35	n.d.	n.d.	n.d.	n.d.
Nd	1.4 ±0.07	2.05 ±0.06	1.13 ±0.17	0.85 ±0.04	0.04 ±0.01	0.02 ±0	0.12 ±0.01	0.04 ±0.01	0.05 ±0.01	0.29 ±0.03	1.71 ±0.6	0.05 ±0.02	0.12 ±0.01	0.03 ±0.01	4.43 ±0.35	6.5 ±0.19	0.03 ±0	0.95 ±0	0.64 ±0	2.4 ±0.31	0.26 ±0.18	0.24 ±0.08	4.04 ±0.17	0.1 ±0.09
Sm	1.33 ±0.1	1.76 ±0.19	0.86 ±0.08	0.72 ±0.08	0.05 ±0	0.03 ±0	0.13 ±0.03	0.04 ±0	0.07 ±0.01	0.28 ±0.01	1.49 ±0.56	0.05 ±0.01	0.12 ±0.01	0.03 ±0.01	4.13 ±0.29	6.25 ±0.28	0.08 ±0	1.19 ±0	0.87 ±0	2.83 ±0.45	0.41 ±0.19	0.37 ±0.1	5.29 ±0.39	0.17 ±0.09
Eu	1.82 ±0.04	5.91 ±0.29	2.34 ±0.19	1.15 ±0.07	0.03 ±0	n.d.	n.d.	n.d.	n.d.	0.22 ±0.02	3.28 ±1.02	0.05 ±0.02	0.09 ±0.04	n.d.	7.51 ±0.64	11.18 ±1.41	n.d.	n.d.	n.d.	n.d.	0.38 ±0.29	0.43 ±0.08	3.36 ±0.21	0.1 ±0.07
Gd	0.96 ±0.17	0.99 ±0.07	0.51 ±0.03	0.53 ±0.02	0.04 ±0	n.d.	n.d.	n.d.	n.d.	0.17 ±0.01	0.93 ±0.37	0.03 ±0.01	0.3 ±0.25	n.d.	3.03 ±0.27	4.81 ±0.47	n.d.	n.d.	n.d.	n.d.	0.38 ±0.08	0.37 ±0.31	4.08 ±0.52	0.19 ±0.1
log (f_{O2}) (ΔIW)	-0.6	-0.47	-0.86	-3.18	-3.4	-1.47	-3.26	-2.81	-3.58	-3.48	-0.68	-1.51	-0.59	-1.51	-0.63	-0.2	-1.38	-2.67	-3.16	-3.42	-0.82	-3.11	-3.95	-3.46

Table S1. Chemical analysis of the run products. Totals in silicate consider only major oxides, and only S-rich phase for the metallic phase when demixion in the Fe–S–Ni–C system occurs (see Appendix A2).
All the reported experiments were performed using the Hvittis based composition. Pressure uncertainties are estimated to be ±0.5 GPa of the reported values and temperature uncertainties are within ±100 K. Oxygen fugacities relative to Iron–Wüstite buffer assuming that γFeO = 1.5, and γFe is calculated using the interaction parameters approach.
Gr: Graphite; MgO: MgO single crystal.
* For samples embedded in graphite capsules, the maximum C contents in Fe-alloys is estimated from the deviation of the analyses totals from 100%.

Appendix A2.

Role of graphite and MgO single-crystal capsules

For experiments with graphite capsules, and for S-rich experiments, we observed the coexistence of two immiscible liquids in the run products for the experimental conditions investigated here (see Figure below). For instance, the experiment performed at 6±1 GPa (run #699) shows the coexistence of a S-rich liquid and a S-poor liquid. The chemical analyses of both phases are as following:

	S-rich phase	S-poor phase
Fe	67.94 ± 1.62	88.35 ± 0.41
Ni	4.46 ± 1.34	3.26 ± 0.18
S	25.30 ± 2.23	2.37 ± 0.08
Si	0.10 ± 0.03	0.06 ± 0.02
Cr	0.02 ± 0.01	0.03 ± 0.01
Total	97.82 ± 0.35	94.07 ± 0.38
Estimated C (wt%)	2.18 ± 0.35	5.93 ± 0.38

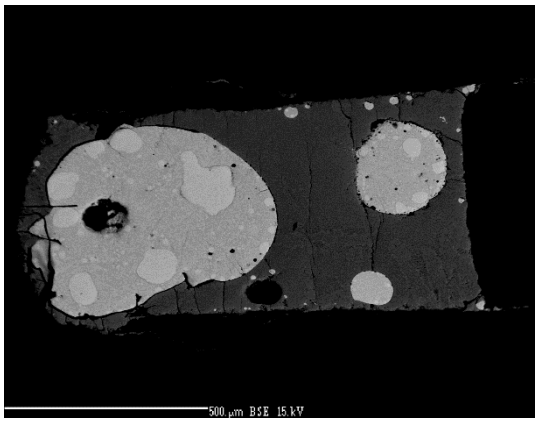

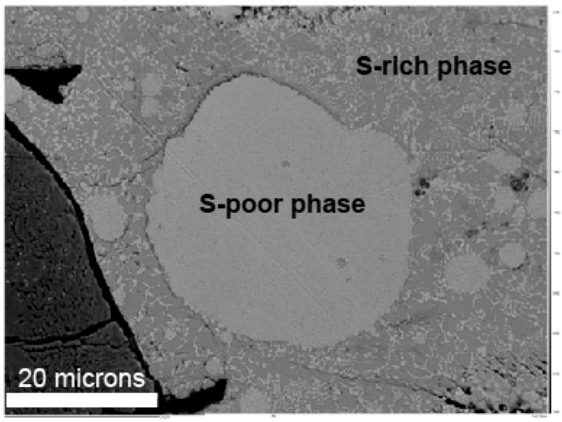

Figure A2-1. Back-scattered electron image of a run-product recovered from 6±1 GPa and 2439 K showing a coexistence in the metallic phase of S-rich and S-poor molten alloys.

The presence of carbon into the metallic phase is due to C diffusion from the graphite capsule into the sample. Observations of a demixion in the Fe–S–Ni–C system are consistent with an immiscibility gap in the Fe–C–S system reported previously for pressures below 5.5 GPa (*e.g.* Corgne *et al*., 2008; Dasgupta *et al*., 2009).

By reporting the C content (for experiment with low Si content < 1 wt%) versus the S content in the metallic phase for all the experiments in the present study (we estimated the C content as the deviation of the analyses totals from 100%). We found that our semi-quantitative C-analyses are compatible with a decrease of the C-solubility with increasing S-content in the metallic liquid.

Also C and Si contents of the metallic phase appear inversely correlated. These trends are consistent with previous experimental studies (Wang et al., 1991; Corgne et al., 2008; Dasgupta and Walker, 2008; Mann et al., 2009) and thermodynamic models at 1 bar (Bouchard and Bale, 1995).

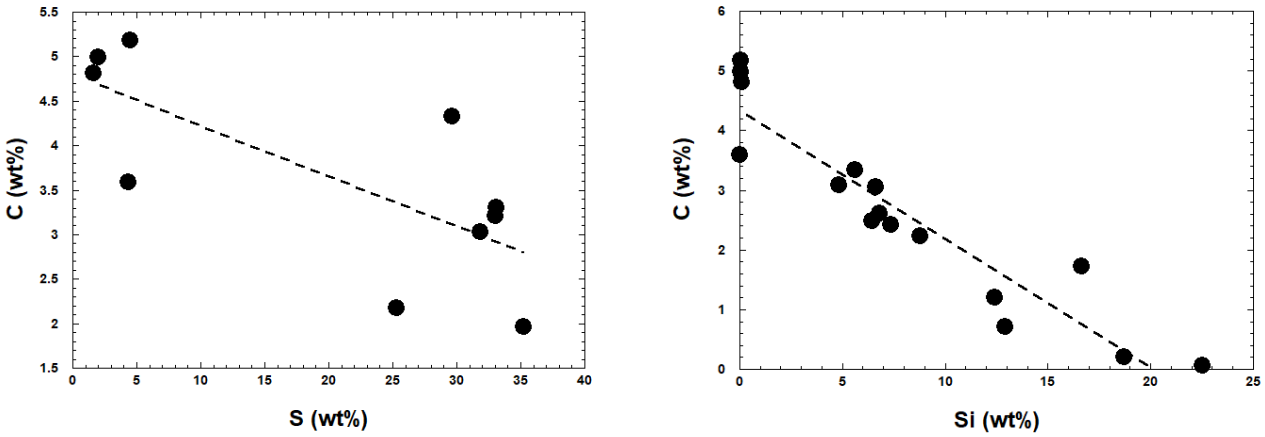

Figure A2-2. C (wt%) vs S (wt%) and C (wt%) vs Si (wt%) for run-products with low Si content, and with low S content, respectively.

Low totals for the run-products with MgO single-crystal capsules

For two experiments with MgO capsules, we performed more than 20 chemical analyses and the Total in average is 97.33 ± 0.25. As reported in the back-scattered electron image below this is related to the state of the surface of the run-product that shows high level of porosity.

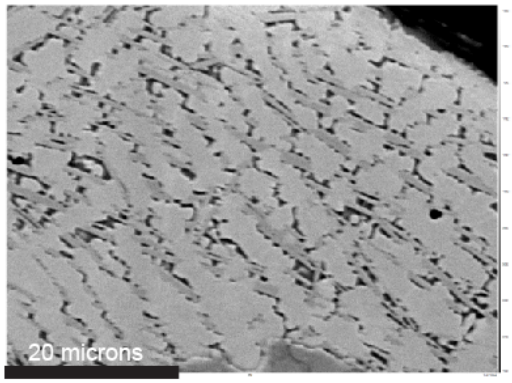

Figure A2-3. Back-scattered electron image of the metallic phase for a run-product recovered from 14±1 GPa, 2560 K, and using MgO as capsule.

Appendix B. Effect of the nature of the capsule (C or MgO) on Sm and Nd partition coefficients in our experiements. The experiments were performed in similar conditions (from 2450 to 2560 K, at ~IW–1.5 in sulphur free environment), with the exception of pressure conditions. Error bars display 1 sigma uncertainties, showing no significant impact of the nature of the capsule or pressure on the resulting partition coefficients.

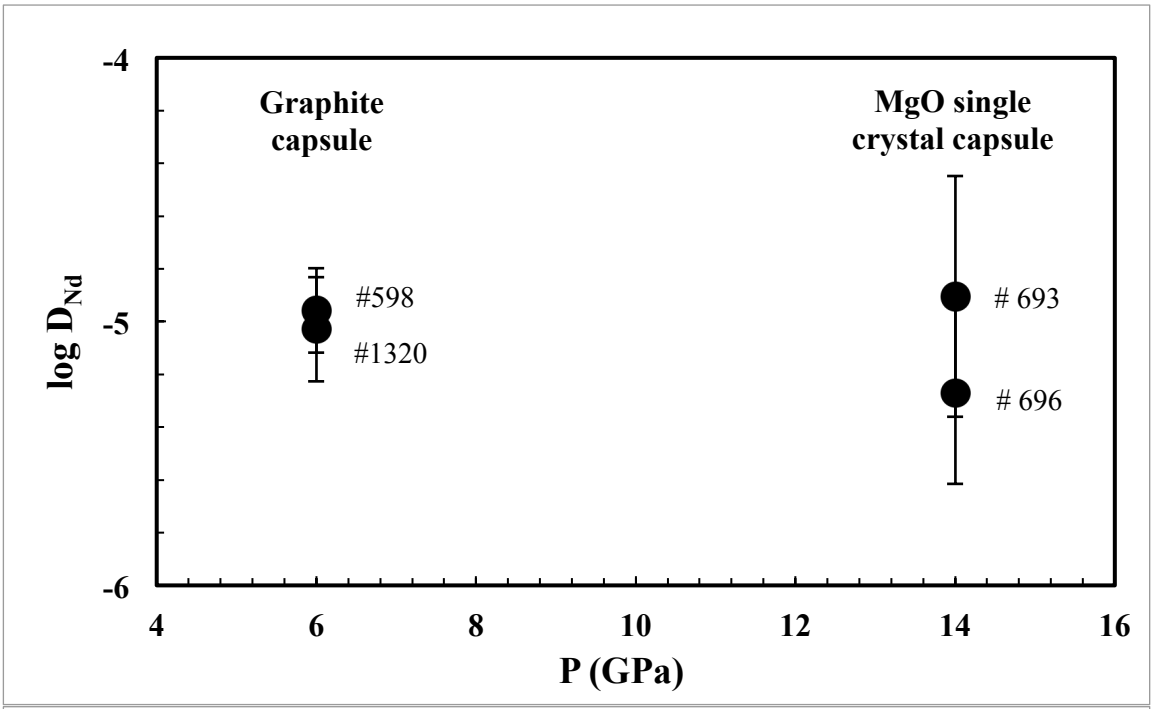

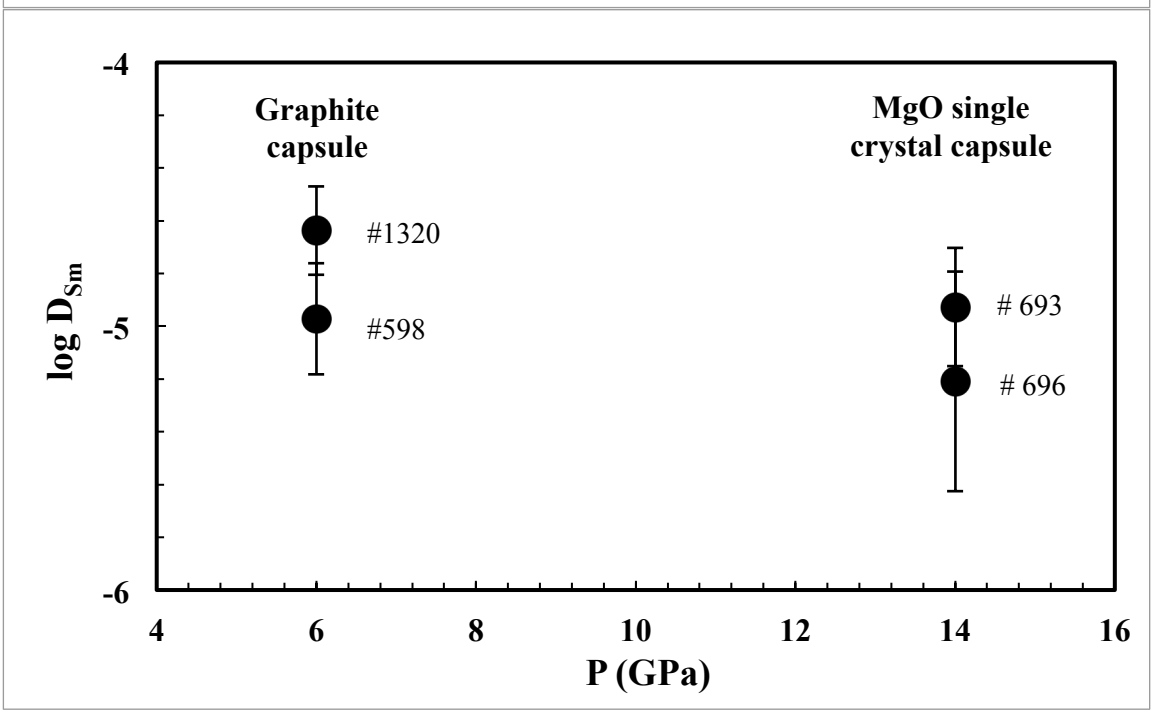

Appendix C. Compilation of experimental data

Run	*Capsule*	*P (GPa)*	*T (K)*	*log fO_2 (ΔIW)*	*NBO/T*	*$X_{S\ metal}$ (wt%)*	*D_{La}*	*D_{Ce}*	*D_{Pr}*	*D_{Nd}*	*D_{Sm}*	*D_{Eu}*	*D_{Gd}*
						Bouhifd et al., 2015							
969	Gr	4	2128	-1.43	3.61	0.00				4.13×10^{-5}	4.43×10^{-5}		
975	Gr	4	2073	-1.56	2.30	0.00				5.05×10^{-5}	5.38×10^{-5}		
1026	Gr	5	2273	-0.82	2.29	23.79				1.08×10^{-3}	1.12×10^{-3}		
1027	Gr	5	2273	-4.42	2.30	0.00				1.60×10^{-3}	2.06×10^{-3}		
986	MgO	6	2173	-1.64	2.08	0.00				5.12×10^{-5}	6.14×10^{-5}		
1021	MgO	6	2173	-1.44	2.35	21.53				2.69×10^{-4}	3.75×10^{-4}		
1028	MgO	8	2373	-1.45	2.16	19.10				3.00×10^{-4}	2.75×10^{-4}		
1029	MgO	8	2373	-4.67	2.14	0.00				4.79×10^{-3}	5.44×10^{-3}		
1082	Gr	5	2023	-4.60	0.52	0.00				2.52×10^{-2}	3.01×10^{-2}		
1137	Gr	5	1973	0.90	1.73	35.31				1.18×10^{-3}	7.73×10^{-4}		
						Wohlers and Wood., 2017							
701	Gr	1.5	2373	-0.78	0.80	28.94	1.06×10^{-2}			1.10×10^{-2}	9.92×10^{-3}	1.87×10^{-2}	
700	Gr	1.5	2373	-3.73	0.24	34.50	3.94×10^{-1}	5.00×10^{-1}		4.81×10^{-1}	4.75×10^{-1}	2.19×10^{-1}	
699	Gr	1.5	2373	-3.89	0.43	35.49	2.02×10^{-1}	1.43×10^{-1}		2.35×10^{-1}	2.45×10^{-1}	2.29×10^{-1}	
697	Gr	1.5	2373	-3.95	0.25	35.73	3.28×10^{-1}	5.00×10^{-1}		3.80×10^{-1}	$3.78E\times10^{-1}$	2.17×10^{-1}	
						Ingrao et al., 2019							
1266		8.50E-06	1573	-4.10		36.88	1.70×10^{-2}	2.40×10^{-2}	3.00×10^{-2}	2.80×10^{-2}	4.50×10^{-2}	9.00×10^{-2}	2.40×10^{-2}
1282		7.00E-08	1573	-4.50		36.56	3.40×10^{-2}	3.20×10^{-2}	4.30×10^{-2}	3.10×10^{-2}	4.10×10^{-2}	1.22×10^{-1}	2.00×10^{-2}
1207		9.00E-07	1673	-4.80		38.23	3.86×10^{-1}	4.81×10^{-1}	4.25×10^{-1}	3.99×10^{-1}	3.27×10^{-1}	6.58×10^{-1}	1.52×10^{-1}
1239		8.50E-07	1673	-4.80		36.48	5.50×10^{-2}	5.70×10^{-2}	4.80×10^{-2}	5.30×10^{-2}	5.10×10^{-2}	7.40×10^{-2}	3.00×10^{-2}
1284		7.00E-08	1673	-5.80		36.66	2.40×10^{-2}	2.80×10^{-2}	2.60×10^{-2}	2.40×10^{-2}	1.90×10^{-2}	2.70×10^{-2}	9.00×10^{-3}
1252		1.00E-06	1673	-5.80		36.56	2.72×10^{-1}	3.68×10^{-1}	4.06×10^{-1}	3.34×10^{-1}	2.96×10^{-1}	5.98×10^{-1}	1.40×10^{-1}

Appendix C. (continued)

Run	*Capsule*	*P (Gpa)*	*T (K)*	*log fO_2 (ΔIW)*	*NBO/T*	*$X_{S\ metal}$ (wt%)*	*D_{La}*	*D_{Ce}*	*D_{Pr}*	*D_{Nd}*	*D_{Sm}*	*D_{Eu}*	*D_{Gd}*
						Lodders (1996)							
EQ6	Gr		1473	2.36		43.7	1.00×10^{-2}		1.00×10^{-2}		9.00×10^{-3}	6.50×10^{-2}	5.00×10^{-3}
EQ1	Gr		1483	2.46		43.6	9.00×10^{-3}		9.00×10^{-3}	7.50×10^{-3}	5.50×10^{-3}	4.40×10^{-2}	5.80×10^{-3}
VQ1	Gr		1473	2.26		43.56	1.50×10^{-2}		1.60×10^{-2}	1.70×10^{-2}	1.40×10^{-2}	6.60×10^{-2}	1.40×10^{-2}
VQ2	Gr		1473	2.36		39.5	5.60×10^{-3}		6.00×10^{-3}	8.00×10^{-3}	4.60×10^{-3}	3.90×10^{-2}	3.00×10^{-3}
VQ4	Gr		1473	0.26		36	4.10×10^{-3}		3.50×10^{-3}		3.70×10^{-3}	6.00×10^{-3}	2.80×10^{-3}
VQ3	Gr		1473	-1.44		33.6	1.30×10^{-3}		1.20×10^{-3}		1.30×10^{-3}	7.00×10^{-3}	
EQ9	Gr		1473	-2.74		37.65	2.90×10^{-1}		3.30×10^{-1}	2.50×10^{-1}	1.70×10^{-1}	8.50×10^{-1}	8.10×10^{-2}
EQ10	Gr		1473	-2.84		14.71	4.80×10^{-1}		5.10×10^{-1}	3.80×10^{-1}	2.00×10^{-1}	1.08	1.40×10^{-1}
EQ4	Gr		1473	0		33.9	1.40×10^{-3}		1.00×10^{-3}		7.00×10^{-4}	3.50×10^{-3}	
EQ3	Gr		1473	-0.34		35	6.00×10^{-4}					3.00×10^{-3}	
QR1	Gr		1473	1.76		44.45	3.10×10^{-2}				1.60×10^{-2}	1.15×10^{-1}	
QR2	Gr		1473	2.16		40.42	3.80×10^{-2}				2.50×10^{-2}	1.64×10^{-1}	

Table S2. Compilation of the experimental data used to derive the coefficients of equation (4) for all studied REE. The uncertainties on the reported data can be found in the original papers.

Appendix D. Effect of experimental conditions on REE metal-silicate partition coefficients.

D.1 Evolution of D_{REE} with $\log fo_2$. Presented results are from this study (Appendix A) and from literature (Apprendix B). Data are corrected from the effect of metalic sulphur, using the parametrization presented in equation 6 and Table 2.

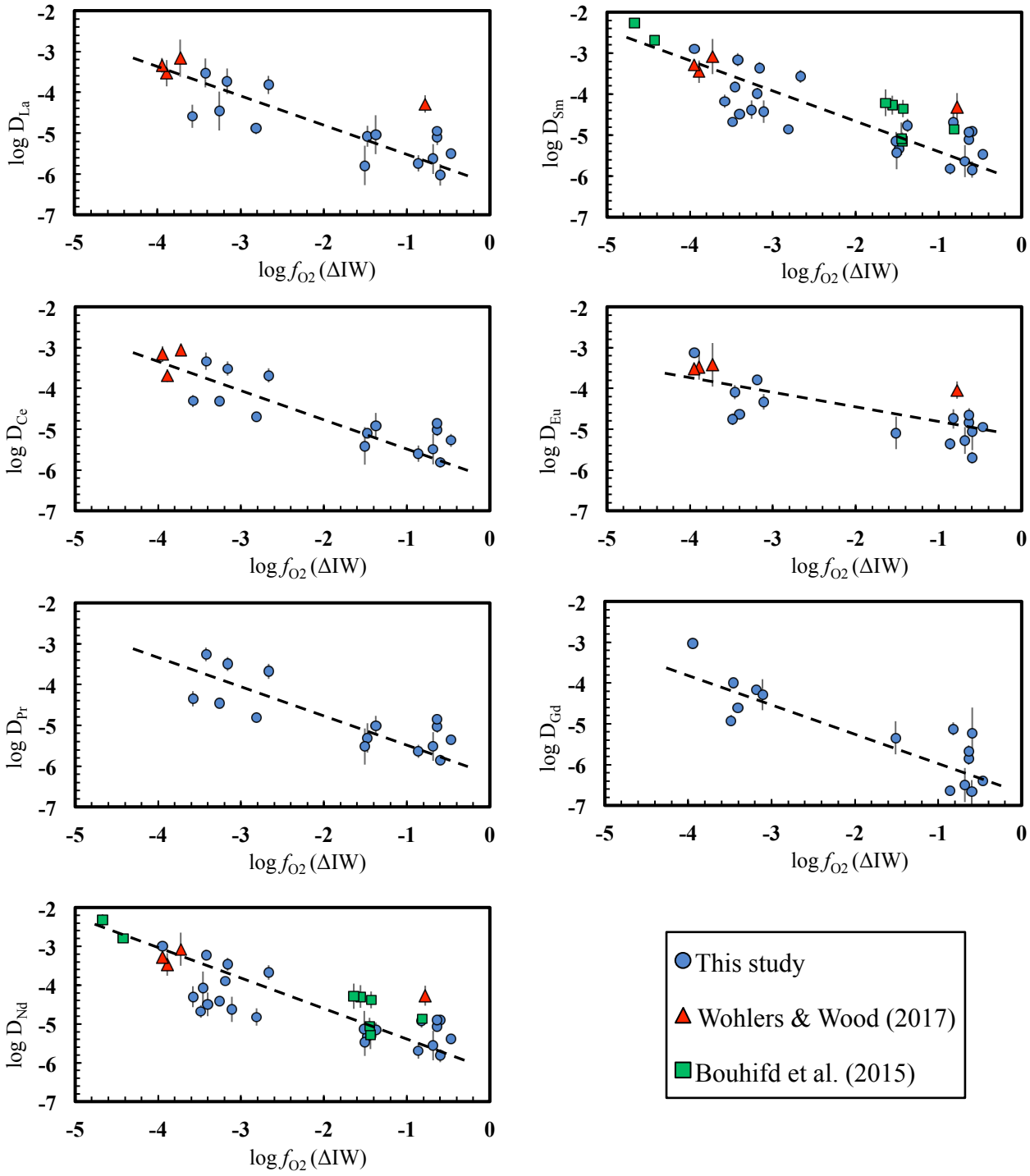

Appendix D.2 Evolution of D_{REE} with the S concentration in the metal. Presented results are from this study (Appendix A) and from literature (Apprendix B). Data are corrected for the effect of oxygen fugacity, using the parametrization presented in equation 6 and Table 2.

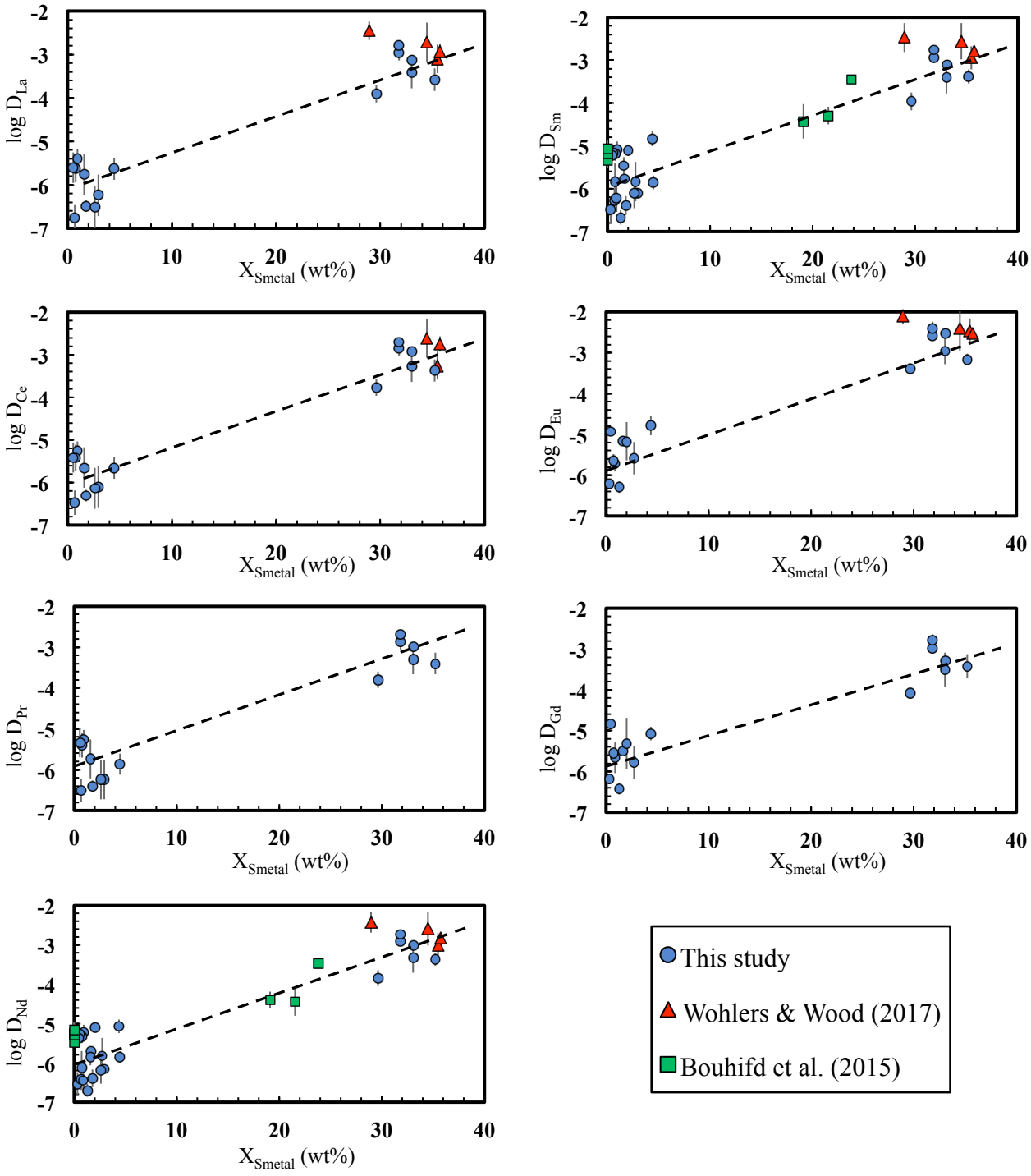

Appendix D3. Effect of temperature on metal - silicate partitioning of REE

In the following, we will use Nd as an example to determine the effect of temperature on metal-silicate partitioning of the REE.

The metal - silicate partitioning of Nd is shown relative to that of Fe in terms of an exchange reaction:

$Nd_2O_{3(silicate)} + 3\ Fe_{(metal)} = 2\ Nd_{(metal)} + 3\ FeO_{(silicate)}$

The free energy of the reaction $\Delta G_{reaction} = \Delta H_{reaction} - T\Delta S_{reaction}$

where $\Delta H_{reaction}$ and $\Delta S_{reaction}$ are the enthalpy and the entropy of the reaction, respectively.

$\Delta H_{reaction} = 3\ H_{formation}\ (FeO) - H_{formation}\ (Nd_2O_3)$

Using tabulated values of $H_{formation}$ (FeO) from Robie and Hemingway (1995); and those of Gschneidner et al. (1973) and Barin et al. (1989) for Nd_2O_3, a value of approximately 1000 kJ/mol is obtained for $\Delta H_{reaction}$ at 2000 K.

In addition, $\Delta S_{reaction} = 2\ S\ (Nd) + 3\ S\ (FeO) - S\ (Nd_2O_3) - 3\ S\ (Fe)$.

Using tabulated values of Barin et al. (1989) for Nd, of Gschneidner et al. (1973) and Barin et al. (1989) for Nd_2O_3, and of Robie and Hemingway (1995) for Fe and FeO, a value of approximately 100 J/mol K is obtained for $\Delta S_{reaction}$ at 2000 K.

Therefore, the term $T\Delta S_{reaction}$ is about one order of magnitude lower than the term $\Delta H_{reaction}$. Varying the temperature in the likely range during core formation (2500 to 3500 K), will result in a small change on $\Delta G_{reaction}$. From this, and considering that the effect of temperature on $\Delta H_{reaction}$ is negligible, we conclude that temperature should not affect metal-silicate partitioning of Nd, and, by extension, all REE.

Appendix E. Accretion model.

We present here models of planetary accretion focusing on the evolution of the REE (La to Gd) content of the different reservoirs (core, bulk silicate Earth) during metal-silicate differentiation.

At each step of accretion (1% M_E), the impactor's metal and silicate equilibrate within the proto-mantle, which represents 68% of planet's mass throughout the entire accretion. Equilibration pressure is set at a pressure of 50% of the core-mantle boundary at each step. This fraction is derived from previous studies on the partitioning of siderophile elements sensitive to pressure (*e.g.* Boujibar et al., 2014; Fischer et al., 2015), leading to a final equilibration pressure set at 60 GPa (Siebert et al., 2012). Temperature is fixed at the liquidus of chondritic melts given in Andrault et al., (2011), evolving from 1900 K when the proto-Earth is at 1% of its final mass up to 3500 K in the final stage of accretion. The oxygen fugacity is constrained to the fO_2 paths defined in Clesi et al., (2016), into a range going from IW-5 to IW-2. All scenarios studied here reproduced within error, the Earth primitive mantle $fO_2 \approx \Delta$IW-2.3.

Each increment of the model represent the growth of the proto-Earth of 1% of its final mass, by the arrival of impactors already differentiated into silicate mantles and metallic cores (Taylor and Norman, 1990). The initial chemical compositions of impactors are those measured on various types of chondrites, depending of the studied scenarios chondrites mixtures (Wasson and Kallemeyn, 1988; see below for REE). The compositions of both metal and silicate reservoirs are calculated at 1 GPa and 2000 K for every element studied here, using their respective partition coefficients. The metal silicate equilibration takes place at fO_2 conditions coherent with the type of chondrites attributed to each accretion step, ranging from ~ IW -4 to IW (Brett and Sato, 1984). In any way, the silicate reservoir of the impactor

contains the near total of all REE because the differentiation leads to a maximum of a few ppb of the studied REE in the metallic phase.

Partitioning is determined using our parameterizations from Table 2. Following the approach of Deguen et al. (2014), we take into account the effect of partial metal–silicate equilibration on element partitioning, which is mainly effective during the final 40% of Earth's accretion. We apply here the method detailed in Rubie et al. (2011) in order to reproduce the metal-silicate partial equilibration by modeling an exponential decrease of the equilibration rates during the last stage of accretion (see equation 4 of Rubie et al., 2011). We consider that the equilibration between the proto-Earth's mantle and the metal of the impactor becomes less efficient as the accretion progresses (*e.g*. Deguen et al., 2014; Rubie et al., 2015). For the last giant impact that formed the Moon (M_I=0.1M_E), the impactor's core merges almost completely with the Earth's proto-core, with less than 5 % of its mass equilibrating with the silicate mantle. Due to the lithophile behavior of REE, the impact of equilibration on our results is very limited, in agreement with Rudge et al., (2010). At each step of accretion, the content of the metallic core in Ni, O and Si is defined using the parametrisations of Fischer et al. (2015). The C content of the core remains constant at 0.2 wt% during accretion (Wood et al., 2006), and a late addition of sulfur-rich material increases the S content of the core to 2 wt% to fit geophysical, geochemical, and experimental estimates (e.g., Allègre et al., 1995; Boujibar et al., 2014; Dreibus and Palme, 1996; Palme and O'Neill, 2003, Suer et al., 2017). Variations of the O and Si contents in the metal are related to the proportion of reduced and oxidized building blocks, which influence the fo_2 path. In models that consider a fully accreted Earth built from a major proportion (80%) of reduced materials, the Earth's core contains 0.2 wt% C, 2 wt% S, 6.75 ± 0.75 wt% Si, and 2.8 ± 0.7 wt% O. However the incorporation of these light elements into the core lead to a negligible enrichment (no more than 1.3%) of the silicate reservoir in REE.

In order to use the most precise and up-to-date REE concentrations for the various types of chondrites proposed as building blocks for the Earth, we compiled data from the most recent publications. The lowest concentrations in REE among the different groups of chondrites are measured in CI and enstatite chondrites whereas the most enriched are those of the CV group (factor 2). For the EL subgroup, data on EL3 from Barrat et al. (2014) are considered. Most EL samples belong to the EL6 subgroup and show depletion in light REE relative to heavy REE due to melting and thermal metamorphism events (Barrat et al., 2014; Boyet et al., 2018; Rubin et al., 2009). Concentrations used in this model are presented in the table below (Table S3), along with the enrichment factor f_{dry} which is applied to the REE concentrations in order to take volatile depletion observed on Earth compared to chondrites into account (for details see text).

	La	**Ce**	**Pr**	**Nd**	**Sm**	**Eu**	**Gd**	f_{dry}	***references***
EH	222 ±17	575 ±35	86 ±5	433 ±21	138 ±6	52 ±2	194 ±12	***1.59***	*Barrat et al., 2014* *Dauphas and Pourmand 2015* *Boyet et al.,2018*
EL	250 ±53	650 ±120	100 ±18	509 ±87	166 ±31	59 ±7	235 ±33	***1.61***	
CI	248 ±26	637 ±58	98 ±42	496 ±35	161 ±10	61 ±4	221 ±16	***2.39***	*Barrat et al., 2012* *Braukmuller et al., 2018* *Pourmand and Dauphas., 2012* *Dauphas and Pourmand., 2015*
CV	475 ±45	1194 ±113	188 ±8	963 ±72	309 ±25	108 ±6	411 ±34	***1.69***	*Braukmuller et al., 2018* *Dauphas and Pourmand., 2015*
CO	363 ±104	949 ±242	151 ±27	784 ±105	255 ±29	96 ±12	362 ±9	***1.67***	
CM	294 ±33	772 ±79	122 ±12	620 ±61	203 ±19	77 ±7	315 ±51	***2.02***	
H	397 ±146	957 ±229	142 ±32	700 ±135	216 ±32	81 ±6	289 ±37	***1.62***	*Dauphas and Pourmand., 2015*
L	324 ±53	908 ±218	135 ±31	683 ±155	217 ±47	83 ±9	290 ±56	***1.69***	
LL	434 ±181	1134 ±476	168 ±69	844 ±338	265 ±102	91 ±9	352 ±130	***1.77***	

Table S3. REE concentrations (in ppb) for chondrite groups used in our calculation, taken from the most recent published trace element measurements on chondrites. f_{dry} corresponds to the enrichment factor applied to concentrations of REE presented here in order to take the volatile depletion observed on Earth relative to chondrites into account.

Appendix References

Andrault, D., Bolfan-Casanova, N., Nigro, G.L., Bouhifd, M.A., Garbarino, G., and Mezouar, M. (2011). Solidus and liquidus profiles of chondritic mantle: Implication for melting of the Earth across its history. Earth and Planetary Science Letters *304*, 251–259.

Barin, I., Sauert, F., Schultze-Rhonhof, E., Sheng, W.S. (1989) Thermochemical Data of Pure Substances, Part I and Part II, CH Verlagsgesellschaft, Weinheim, Germany. 1739 pp.

Barrat, J.A., Zanda, B., Jambon, A., and Bollinger, C. (2014). The lithophile trace elements in enstatite chondrites. Geochimica et Cosmochimica Acta *128*, 71–94.

Bouchard, D. and Bale, C.W. (1995) Simultaneous optimization of thermochemical data for liquid iron alloys containing C, N, Ti, Si, Mn, S, and P. Metall. Mater. Trans. B *26*, 467–484.

Boujibar, A., Andrault, D., Bouhifd, M.A., Bolfan-Casanova, N., Devidal, J.-L., and Trcera, N. (2014). Metal–silicate partitioning of sulphur, new experimental and thermodynamic constraints on planetary accretion. Earth and Planetary Science Letters *391*, 42–54.

Boyet, M., Bouvier, A., Frossard, P., Hammouda, T., Garçon, M., and Gannoun, A. (2018). Enstatite chondrites EL3 as building blocks for the Earth: The debate over the 146 Sm–142 Nd systematics. Earth and Planetary Science Letters *488*, 68–78.

Brett R. & Sato M. (1984) Intrinsic oxygen fugacity measurements on seven chondrites, a pallasite, and a tektite and the redox state of meteorite parent bodies. Geochimica et Cosmochimica Acta *48*, 111–120.

Clesi, V., Bouhifd, M.A., Bolfan-Casanova, N., Manthilake, G., Fabbrizio, A., and Andrault, D. (2016). Effect of H_2O on metal–silicate partitioning of Ni, Co, V, Cr, Mn and Fe: Implications for the oxidation state of the Earth and Mars. Geochimica et Cosmochimica Acta *192*, 97–121.

Corgne, A., Wood, B.J. and Fei, Y. (2008) C- and S-rich molten alloy immiscibility and core formation of planetesimals. Geochim. Cosmochim. Acta *72*, 2409–2416.

Dasgupta, R., Buono, A., Whelan, G. and Walker, D. (2009) High pressure melting relations in Fe–C–S systems: implications for formation, evolution, and structure of metallic cores in planetary bodies. Geochim. Cosmochim. Acta *73*, 6678–6691.

Dasgupta, R. and Walker, D. (2008) Carbon solubility in core melts in a shallow magma ocean environment and distribution of carbon between the Earth's core and the mantle. Geochim. Cosmochim. Acta *72*, 4627–4641.

Deguen, R., Landeau, M., and Olson, P. (2014). Turbulent metal–silicate mixing, fragmentation, and equilibration in magma oceans. Earth and Planetary Science Letters *391*, 274–287.

Fischer, R.A., Nakajima, Y., Campbell, A.J., Frost, D.J., Harries, D., Langenhorst, F., Miyajima, N., Pollok, K., and Rubie, D.C. (2015). High pressure metal–silicate partitioning of Ni, Co, V, Cr, Si, and O. Geochimica et Cosmochimica Acta *167*, 177–194.

Gschneidner, K.A., Kippenhan, N.A., McMasters, O.D. (1973): Thermochemistry of the rare Earths. Rare-Earth Information Center, Institute for Atomic Research, Iowa State University, Ames, Iowa.

Mann, U., Frost, D.J. and Rubie D.C. (2009) Evidence for high pressure core-mantle differentiation from the metal-silicate partitioning of lithophile and weakly-siderophile elements. Geochim. Cosmochim. Acta *73*, 7360–7386.

Robie, R.A., Hemingway B.S. (1995): Thermodynamic properties of minerals and relied substances at 298.15 K and 1 bar (10^5 Pascals) pressure and at higher temperatures. U.S. Geological Survey Bulletin 2131.

Rubie, D.C., Frost ,D.J., Mann, U., Asahara, Y., Nimmo, F., Tsuno, K., Kegler, P., Holzheid, A. & Palme, H. (2011) Heterogeneous accretion, composition and core–mantle differentiation of the Earth. *Earth Planet. Sci. Lett.* **301**, 31–42.

Rubie, D.C., Jacobson, S.A., Morbidelli, A., O'Brien, D.P., Young, E.D., de Vries, J., Nimmo, F., Palme, H., and Frost, D.J. (2015). Accretion and differentiation of the terrestrial planets with implications for the compositions of early-formed Solar System bodies and accretion of water. Icarus *248*, 89–108.

Rubin, A.E., Huber, H., and Wasson, J.T. (2009). Possible impact-induced refractory-lithophile fractionations in EL chondrites. Geochimica et Cosmochimica Acta *73*, 1523–1537.

Rudge, J.F., Kleine, T., and Bourdon, B. (2010). Broad bounds on Earth's accretion and core formation constrained by geochemical models. Nature Geoscience *3*, 439–443.

Siebert, J., Badro, J., Antonangeli, D., and Ryerson, F.J. (2012). Metal–silicate partitioning of Ni and Co in a deep magma ocean. Earth and Planetary Science Letters *321–322*, 189–197.

Taylor, S., and Norman, M. (1990). Accretion of differentiated planetesimals to the Earth. Origin of the Earth *1*, 29–43.

Suer, T.-A., Siebert, J., Remusat, L., Menguy, N., Fiquet, G., 2017. A sulfur-poor terrestrial core inferred from metal–silicate partitioning experiments. Earth Planet. Sci. Lett. *469*, 84–97.

Wang, C., Hirama, J., Nagasaka, T. and Ban-Ya, S. (1991) Phase equilibria of liquid Fe–S–C ternary system. ISIJ International *31*, 1292–1299.

Wasson, J.T., and Kallemeyn, G.W. (1988). Compositions of Chondrites. Philosophical Transactions of the Royal Society A: Mathematical, Physical and Engineering Sciences *325*, 535–544.

Wohlers, A., and Wood, B.J. (2015). A Mercury-like component of early Earth yields uranium in the core and high mantle 142Nd. Nature *520*, 337–340.